# A New Stator Design and Validation of Hollow Cylindrical Piezoelectric Motor

by

Yang Wang

A Thesis

Submitted to the Faculty

of the

WORCESTER POLYTECHNIC INSTITUTE

In partial fulfillment of the requirements for the

Degree of Master of Science

in

Robotics Engineering

by

---

August 2021

APPROVED:

---

Professor Gregory S. Fischer, Major Advisor, RBE Department, WPI

---

Professor Jing Xiao, Committee Member, RBE Department, WPI

---

Professor Haichong Zhang, Committee Member, RBE Department, WPI

**Abstract**

Robot-assisted surgery based on magnetic resonance imaging (MRI) can help surgeons perform operations more precisely with its real time imaging capability. However, the magnetic field within MRI narrows down the available actuators and effectors. Many researches have proved that electrical powered non-ferromagnetic motors based on piezoelectric elements to be well suited for MRI compatible robots, while the planar rotary design will lead to multiple problems, for example: 1) a high excitation frequency will be required to form stable contacts between the rotor and the stator; 2) an additional flange or mechanism will be required to transfer movements to the effector; 3) it may not be able to keep concentric during the rotation of the rotor if additional constraints are not applied to the rotor. In this thesis, we designed and fabricated a customized stator for a piezoelectric actuator that has a hollow cylindrical shape, and validated it with simulation and practical experiments. We first performed a FEM simulation to find the excitation frequencies of the piezoelectric element (PZT-5H) and the displacement of multiple points on the surface of stator assembly where coupling with rotors that we designed. Then, two real stator assemblies with multiple stator prototypes were manufactured to validate the practical performance comparing to the simulation. The performance of the stator assembly matched the simulation result with a maximum error of $\pm 2.6\%$ and an average error of $\pm 0.6\%$ among the second to the fifth excitation modes. The change of performance of the stator assembly while in different excitation mode are also discussed in this thesis.

**Acknowledgements**

I would like to express my gratitude first and foremost to my advisor, Professor Gregory S. Fischer, who provides me with motivation and guidance through out the progress of the research. Thanks to Zhanyue Zhao for coming up with me on this novel topic and guiding me on my research study. Thanks to Dr. Christopher J. Nycz for training my skills of using machine shop at Practice Point. Thanks to ProtoLabs, Inc. for their help on quoting and manufacturing the stator in time. Thanks to people at WPI who helped in manufacture and testing of the stator.

I also appreciated the opportunity that Prof. Fischer provided to join A.I.M. lab. The lab has been a second home for me. I would like to thank every students and staff in the A.I.M. lab for being my colleagues and friends, especially my closest collaborators without whom none of this work would have been possible, Zhanyue Zhao, Dr. Katie Y. Gandomi, and Dr. Paulo A. Calvaho.

I would also like to thank my family and friends for providing me an unwavering support in all my endeavors. I am blessed to have a family who encourages me to pursue my scholars dream.

# Contents

# List of Figures

# List of Tables

# Chapter 1

# INTRODUCTION

The work presented here intends to construct a new MRI compatible actuator, which intends to be a step forward for robot assisted surgeries. The developing pace of the field of surgical robotics has been relatively fast since the first robotics surgical intervention performed in 1985, using a PUMA industrial manipulator. Since then, a great number of surgical robots have been designed, developed, and brought in to operation rooms (OR) to assist surgeons on surgeries. [1–4] However, certain limits for developing a surgical robot are existed, due to not only the dimension and environment of the operation site, but the status of both the surgery and the patient as well.

Throughout the years, as the usage of radiography has been widely accepted all over the world, people started to take the advantage of this precise imaging technique. For example, magnetic resonance imaging (MRI) is a non-invasive imaging technique, uses magnetic field and radio wave to temporarily realign the water molecules and generate 3D images of the scanning area, as shown in Fig. 1.1. [5] Fig. 1.2 presents a 3.0T Premier Signa MRI scanner form General Electric (USA) that WPI owns. There are currently around 11,900 MRI systems are available in the United State. [6]

Over forty million MRI scans were performed in the year of 2019. [7]

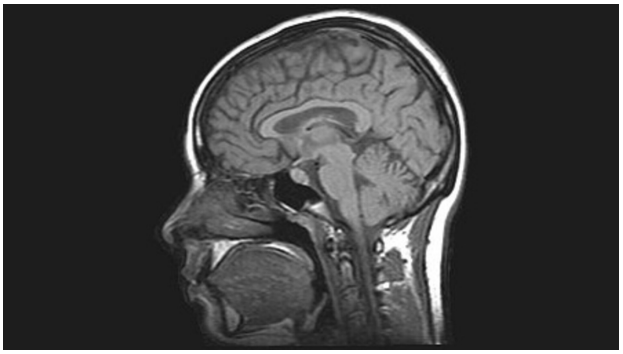

Figure 1.1: A MRI Scan of a Human Brain

Figure 1.2: WPI's GE 3.0T Premier Signa MRI Scanner

The advantage of ultrasound imaging, especially from MRI, has attracted great number of researchers to consider making a regular surgical robot compatible with the scanning machine. Most of the surgical robots are designed to use in a normal OR, as they are using the commonly defined electric actuator to actuate the robot. However, these kind of motors are based on the interaction of the permanent magnetic field and electric current flow within in the coil, as shown in Fig. 1.3. [8] This

kind of motor and the robot equipped with these motors are not sufficient to work with in some severe conditions, such as the high magnetic field within MRI scanner.

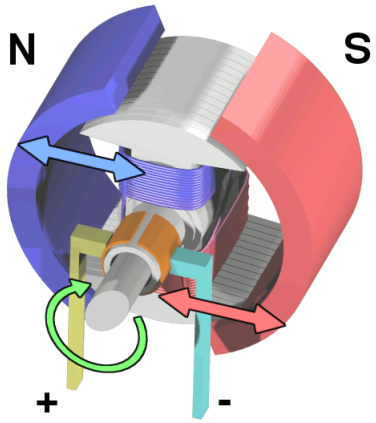


Figure 1.3: Operating Principle of Commonly Defined Electric Motors

MRI-guided surgical robots are robot systems developed to work under the guidance of MRI scanning results. [9–14] Fig. 1.4 shows some examples of the previous MRI-guided surgical robots that were design in the past few decades. Fig. 1.4(a) is a MRI compatible needle insertion robot developed by K. Masamune et al., in 1995. [15] Fig. 1.4(b) presents NeuroArm robot, which was a manipulator that operate under MRI guidance by Sutherland et al. in 2008. [16] Fig. 1.4(c) was presented by Comber et al. in 2014, which was a pneumatically actuated continuum tube robot. [17] A complete MRI-compatible stereotactic neurosurgical robot system was developed by researchers in A.I.M. lab at WPI as shown in Fig. 1.5. [18]

In order to operate these robots in MRI, the robots are equipped with MRI-compatible actuators, which are the different types of actuators that can work within the high magnetic field that MRI machines generate. The operation principles of these actu-

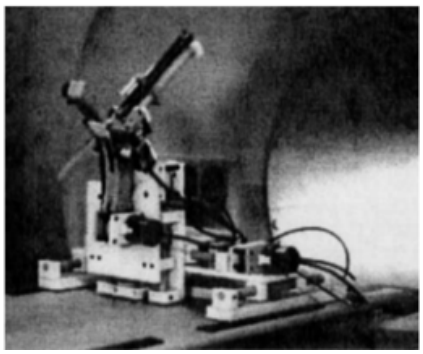

(a) MRI Compatible Needle Insertion Robot

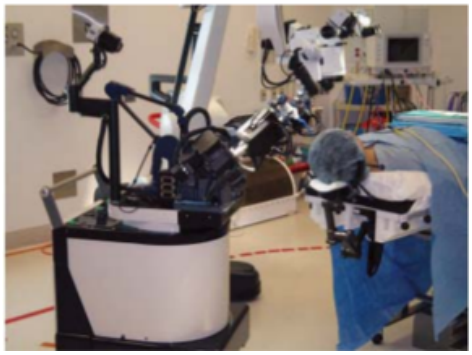

(b) NeuroArm Robot

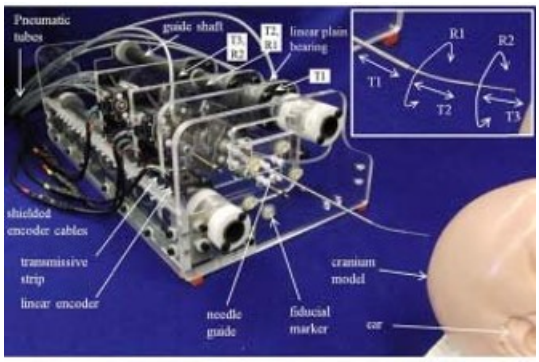


(c) Pneumatically Actuated Continuum Robot

Figure 1.4: Examples of MRI-compatible Surgical Robot Systems

ators are normally based on the characteristics of certain nonferromagnetic materials. There are several type of actuators that can work with MRI: pneumatic actuators [19], hydraulic actuators [20], and piezoelectric actuators [21], electrorheological actuators [22], and electro-strictive polymer actuators [23]. Fig. 1.6 shows some of the MRI-compatible actuators. Pneumatic actuators are using pressurized air or gas to excite motion. Hydraulic actuators are using pressurized liquid. Pneumatic actuator is sufficient to provide high speed of motion, whereas hydraulic actuator is preferred on high load tasks. However, pneumatic and hydraulic actuators cannot provide a high precision control of the motor at some specific circumstances. [24, 25] Thus, these two types of actuator will face up with potential slow reaction time and

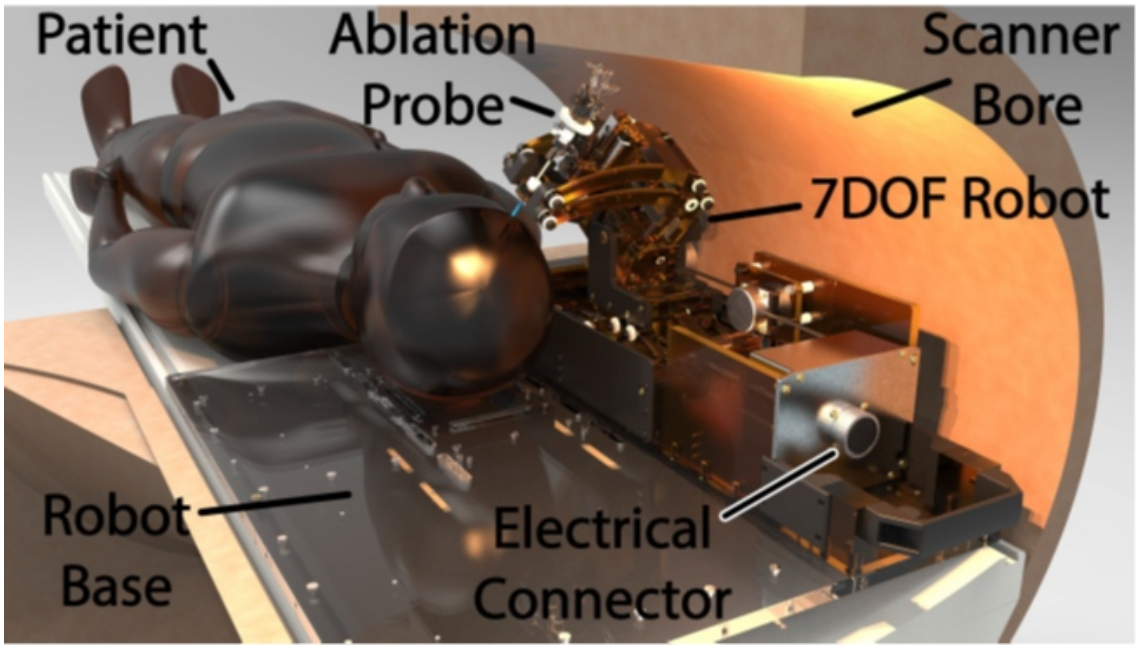


Figure 1.5: Neurosurgical Robot System

leaking issues, due to the operating principle of both designs requires a airflow or liquid pipeline as a connection between the actuator and motion generator. The applications of electrorheological and electro-strictive actuators are mostly focusing on the displacement of a rigid body in a certain range. Piezoelectric actuators have the characteristic that it has faster response time than pneumatic and hydraulic motors, although the torque provided by piezoelectric motor is typically smaller than pneumatic and hydraulic actuators.

For example, the neurosurgical robot we mentioned above was brought to life by seven non-ferromagnetic motors based on piezoelectric element, which are some commercial products, including USR-30 series and USR-60 series, from Shinsei Corporation, Japan, as shown in Fig. 1.7. [29]

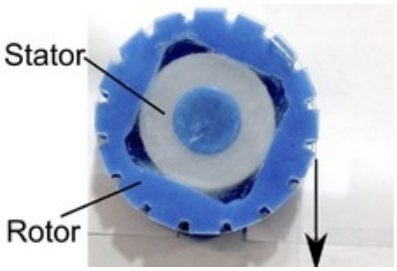


(a) Pneumatic Rotary Actuator [26]

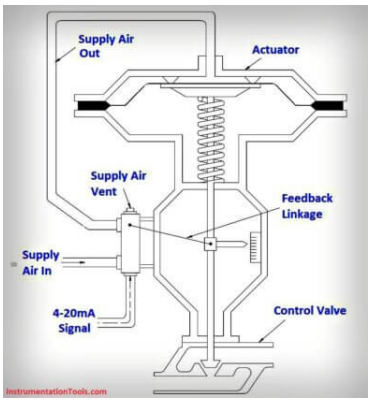


(b) Pneumatic Linear Actuator [27]

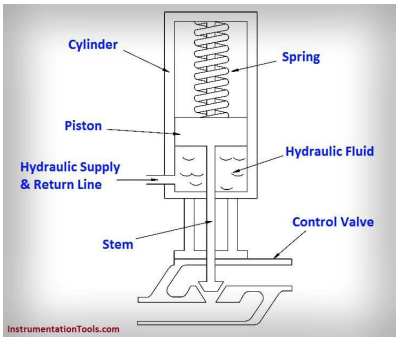


(c) Hydraulic Actuator [20]

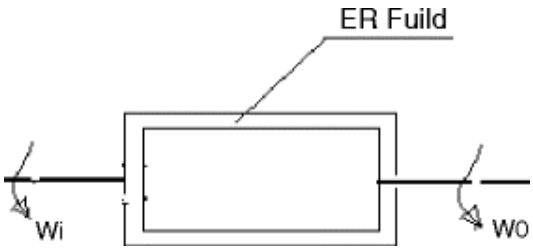


(d) Electrorheological Actuator [22]

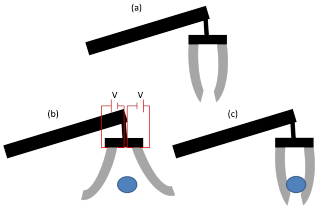


(e) Electro-strictive Polymer Actuator [28]

Figure 1.6: Examples of MRI-compatible Actuators


Figure 1.7: Shinsei USR60-E3

## 1.1 Motivation for Study of Piezoelectric Motor

There are several types of piezoelectric motors including PiezoLegs [30], DTI [31], ultrasonic motor (Shinsei Corporation) [29], and others which are using different means of motion. Fig. 1.8 shows some of the commercially available piezoelectric actuator products. Both PiezoLegs and DTI are focusing on generating linear motion using ultrasonic standing wave, and Shinsei ultrasonic actuators are mainly focused on using ultrasonic traveling wave to generate rotating motion. In this thesis, we focused on ultrasonic traveling wave resonant motors based on Shinsei motors.

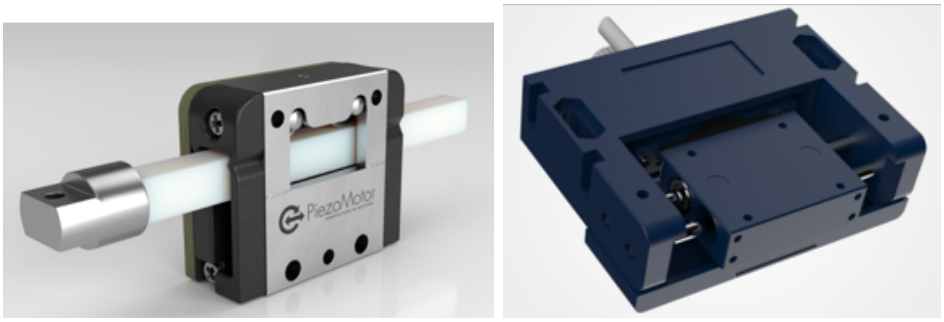


(a) PiezoLegs from PiezoMotor [30] (b) DTI Motor from PiezoMotion [31]

Figure 1.8: Examples of Piezoelectric Actuators

As we can see from Fig. 1.7, current design of most piezoelectric motors is a pla-

nar rotary shape. This kind of planar rotary actuator has a simple design, which means the manufacturing and assembling process is significantly simple. However, this kind of motor requires a steady surface connect on the boundary that shares between the stator and rotor, which means at least a three-point contact will be required to execute the motion of the motor, normally at around 35 kHz. [32]

In order to discuss performance of a piezoelectric actuator, we need to introduce a new term "mode", which is the driving mode of the actuator. An actuator that is at the fifth mode means the mode shape contains five peaks on its tangential surface wave.

According to the previous research on the piezoelectric planar rotary actuators by researchers in A.I.M. at WPI, most of the motor will not be able to perform a constant motion until the fifth mode. [32, 33] Frequencies may be varied due to the material that used to build up the actuator, however, most of the fifth modes occurred around 40kHz in simulation, which is a relatively high frequency. Currently, most of the on the market high voltage power supply can provide signal waves below 50kHz. Due to the manufacture issue and simulation toleration, the frequency might be even higher than expected. In that case, a regular high voltage power supply will not be applicable with the actuator. Thus, exposing in the high frequency noises will lead to potential problems to human's auditory system. From another perspective, higher driving frequencies will also increase the requirement for components, which will also bring up the cost for the whole system.

Comparing to the planar rotary design, a hollow cylindrical style can actuate the motion of the stator at an earlier mode. A shaft will continuously maintaining a steady surface or line contact with the interface of the cylinder, when a shaft penetrates though it with a pre-load from the effector. Imagine a radial force always pointing to the axis on the external side that generates a protruded point which

is moving around the cylinder, friction generated by the moving cycle of the point will bring the shaft into motion. Bring that imagination to our case, the hollow cylindrical piezoelectric motor is expected to be executed even at the first mode.

Beyond the existing problem on the driving frequency side, the planar rotary design also requires a flange or even a gear system to connect the effector. For example, the neurosurgical robot mentioned above has an end-effector which is a probe. Due to the design of the actuator, we have to put the probe a few distance away to fit the gear system in. However, the neurosurgical robot is supposed to work inside the MRI scanner, which is a relatively narrow space.

From the results of the formal experiments on the planer rotary piezoelectric motors, the rotor always stopped after rotating for a short term of time, because it would move to an offset position whereas the torque generated by friction became unbalanced. However, it would continue to rotate if the rotor was touched and pushed to a more concentric position.

However, a hollow cylindrical design will allow the probe to get through the actuator, enable the probability for a direct drive. With that design, a flange or a gear system will no longer be a necessary component for a piezoelectric actuator involved rotary system. Furthermore, the design of a hollow cylindrical stator will reduce the impact that brought by concentric issues.

## 1.2 Piezoelectric Motor

A piezoelectric motor is a type of electric motor instead of using the change of magnetic field, but based on the change in shape of a piezoelectric material when an electric field is applied. Piezoelectric motors use the inverse piezoelectric effect, in which deformation or vibration of the piezoelectric material produces an electric

charge. An electrical circuit makes acoustic or ultrasonic vibrations in the piezoelectric material. Friction is provided by the vibration to execute the linear or rotary motion of the motor.

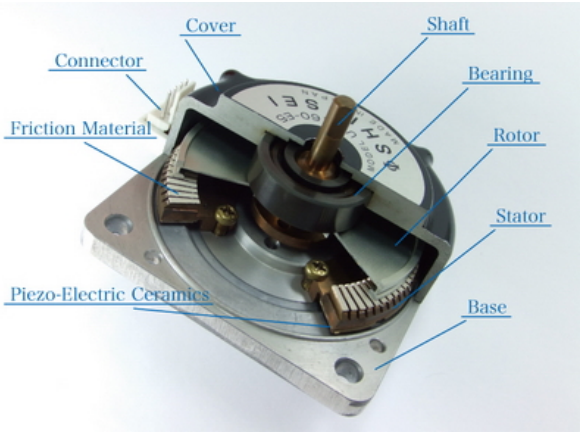


Figure 1.9: Cutaway View of a Shinsei Ultrasonic Motor

Fig. 1.10 indicates the motion principle of a piezoelectric traveling wave ultrasonic motor. For the most occasions, a piezoelectric motor contains several components: base board, piezoelectric element, stator, rotor, and adhesive attachments, as shown in Fig 1.9. [34]

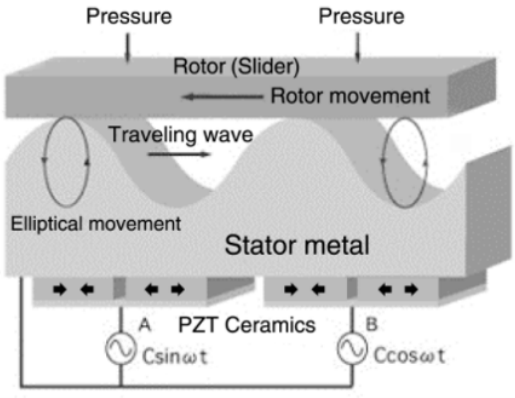


Figure 1.10: Motion Principle of a Traveling Wave Ultrasonic Motor

The piezoelectric ring is adhered underneath the stator using conductive adhesive, which can not only fill up the gap between the stator and piezoelectric ring to transfer the deformation to the stator, but also establish a ground connection for the piezoelectric tube.

### 1.2.1 Piezoelectric Material

Piezoelectric materials are materials that can generates electricity by applying a stress. For example, which is called piezoelectric effect. For example, lead zirconate titanate (also known as PZT), barium titanate, and lithium niobate. The electricity generating effect is called piezoelectric effect. Like the magnetic effect of electric current, the piezoelectric materials also have reverse effect that can cause deformation due to the current flow.

Ultrasonic actuators' motion is occurred based on the motive force that reverse piezoelectric effect generates. The operating principle for piezoelectric motors relies on the characteristic exhibit by some certain materials, which is a mechanical deformation caused by the application of an electric field.

## 1.3 Thesis Contributions

This thesis present the work on developing a stator for a hollow cylindrical piezoelectric motor. A literature review on the hollow cylindrical piezoelectric motor presented in the introductions have showed some previous hollow piezoelectric motor implementations. However, to date, we know of no hollow piezoelectric based on circumferential lateral frictionally coupling method and ultrasonic traveling wave. Thus, comparing to axial polarization, the radial polarization direction that we are designing in this thesis provides more constant motion and precise control.

The key contribution of this thesis is that we design a hollow cylindrical piezoelectric motor inspired by the design of a commercial planar rotary piezoelectric motor from Shinsei Corporation. Comparing to the original piezoelectric motor, the hollow cylindrical design allow multiple types of components to penetrate through, which can help downsizing the system. The motion of our design can be actuated at earlier frequency. This work was initially proposed to replace the insertion and rotation axes on our neurosurgery stereotactic robot, which control the motion of the probe to perform surgeries in human brain. The work was aimed to eliminate the requirement for additional mechanisms and flange to transmit the motion from the motor to the effector. The work also demonstrates a finite element method (FEM) simulation of the stator assembly when the reverse effect of piezoelectric tube was excited. Practical validations on the real motor were performed with various configurations on multiple aspects to compare with simulation results. Furthermore, the application of this novel motor design can be widely applied to all MRI-compatible surgical robots on the rotation axis after future experiment on specifying the characteristic of the motor is performed.

## 1.4 Related Work

There were some researchers working on the development of hollow cylindrical ultrasonic actuators during the past few decades. [35] However, the characteristics of their research are completely different from the method that we are presenting in this thesis. Most of the previous development were based on the axial polarization of the piezoelectric materials. Whereas the stator we presents in this thesis is based on the radial polarization, which is a completely different driving method.

There was a commercial ultrasonic actuator on the market before which comes with

a hollow cylindrical design. The actuator was retired a few years ago, and nearly all paperwork was removed by the company. We listed it below as it has the same designing purpose as ours, however, we can't make sure it was using the same driving method of ours.

### USR60-RN

USR60-RN series [36] is an ultrasonic hollow cylindrical actuator that developed by Shinsei Corporation, Japan, as shown in Fig. 1.11. The ultrasonic actuator is built based on nonferromagnetic materials that can be used in magnetic field environments. The motor is using an axial contacting frictionally coupling method. The maximum torque is 1.0 Nm and can rotate at a maximum speed at 150 rpm. The hollow hole has a diameter of 32 mm, which can penetrate cables, sensors, etc., contributing to downsizing of equipment and realization of new mechanisms.

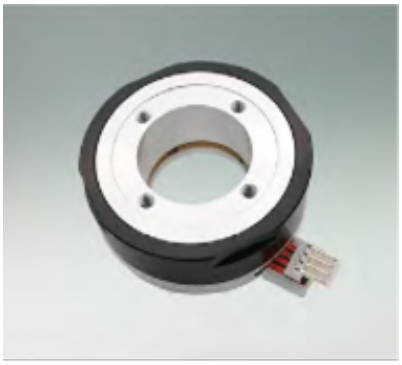

Figure 1.11: USR-60RN Ultrasonic Motor

Characteristics of the USR-60RN series ultrasonic motor can be seen in Appendix B.

## 1.5 Thesis Organizations

The remainder of the thesis is organized as follows:

Chapter 3 presents the methodologies for modeling the stator assembly. Two prototypes of the stator design were clarified and compared at first. With the design model settled, a material selection process for each part based on the material properties and characteristics was provided. Then, the manufacturing process for the parts was also presented, following the design and dimensions from the model.

Chapter 4 introduces the workspace and model configuration for FEM simulation. The model was imported from SolidWorks to COMSOL and configured according our simulation setup. A cylindrical coordinate system was declared with the respect to the default coordinate system configuration. Three boundary probes were applied to the model to observe the displacement while applying the input signals on the piezoelectric tube. An eigen frequency study and a time domain study were added to the model to find out the resonance modes, corresponding frequencies, and estimated performance of the stator. Then three setups were configured to find the impact on the motor performance when changes were made to our proposed stator design.

Chapter 5 demonstrates the physical test of the stator. A validation of the existence of each resonance mode and its corresponding frequency was performed based on the results we received from simulation. Two stator assemblies were fabricated for comparison. A motor performance validation is presented with a rotor installed on the stator. An experiment on the impact of different contacting method was performed. A preload impact experiment is also presented. The issues in this validation process are discussed and possible explanation is declared.

Chapter 6 provides a discussion on the results and issues we gathered during the

whole research process. The results from validation are compared to the simulation, the difference is discussed and possible explanation is proposed.

Chapter 7 summarizes the contribution of the work presented in this thesis, and comes to a conclusion for the whole research process. Some unexpected issues that may affect the result are discussed and future work based on dealing with the problems are proposed.

# Chapter 2

# METHODS

Two designs were proposed when we first conceived the idea of designing a hollow cylindrical motor. Both designs were using a coupling method to achieve a hollow cylindrical design, however, different design makes the motor varies in driving methods.

The first design was using internal coupling which allows the shaft penetrate directly through the center of the motor, as shown in Fig. 2.1. The piezoelectric tube is attached to the outer surface of the stator. The deformation of the tube will be transferred to the center of the stator by the notches on the stator. For this design, a hollow shaft is required to serve as rotor and the carrier of the probe. It will be named as internal actuator in this thesis. This kind of design is easy for fabricating and effectively downsize the motor. However, manufacturing the notches on the inner surface of the stator would be the most difficult topic.

The other design was using external coupling concept, as shown in Fig. 2.2. Unlike the internal actuator, the piezoelectric tube will be attached to inner surface of the stator. In that case, the deformation will be transferred to the notches on the outer

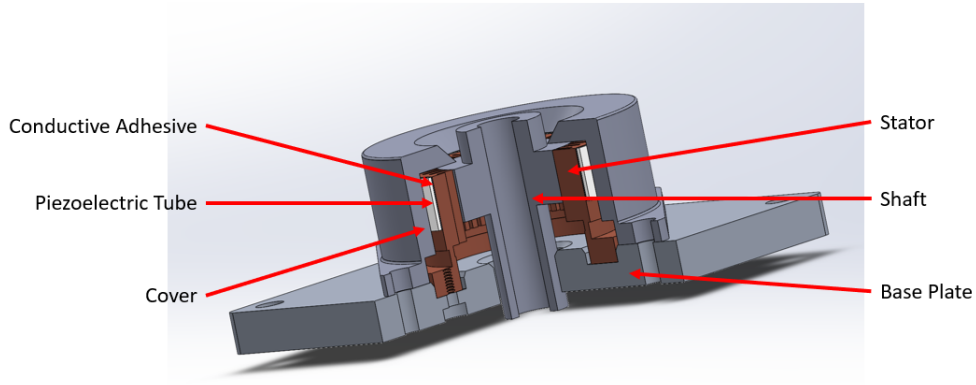


Figure 2.1: A Prototype Design of Internal Piezoelectric Actuator

surface of the stator. A cover-like rotor will be required to deliver the motion to the effector. Notches on the outer surface of the stator means it would be easier to be manufactured, however, the cover-shape rotor that surrounds the stator would be a dedicated mechanism. It would increase the difficulty when fabricating as well due to the power supply need to be soldered to the electrodes which are located on the inner side of the piezoelectric tube. The cover type rotor also requires additional contacting surface between the stator and rotor, which may increase the friction that preventing the rotor from moving. Thus, the rotor will also increase the preload.

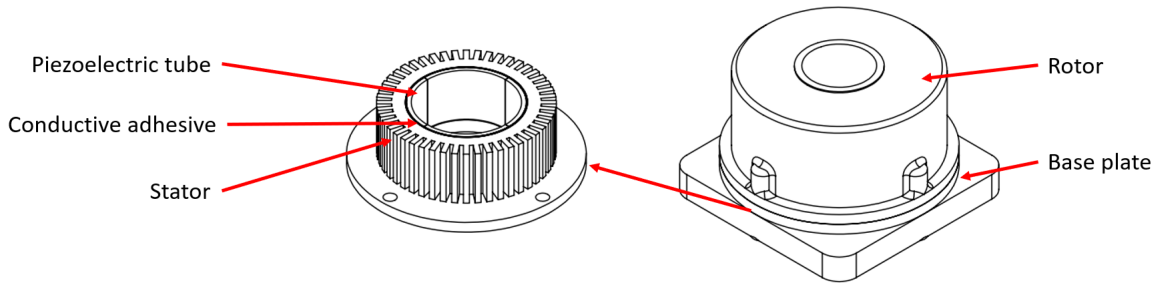


Figure 2.2: A Prototype Design of External Piezoelectric Actuator

In this thesis, the design of the rotor was based on the concept of internal actuator.

## 2.1 CAD Modeling

SolidWorks® 2020 (SolidWorks) was used to draw the cad models. As the purpose of this thesis was to design and validate a stator for hollow cylindrical piezoelectric actuators, only the stator assembly was considered at this time. The render and dimension of the assembly are shown as Fig. 2.3. The cutaway view of the stator assembly is shown in Fig. 2.4. The total dimension of the assembly is 1.5" (length) × 1.5" (width) × 0.63" (height). In this assembly, a stator was designed based on the simulation for the difference when changing the height of the piezoelectric tube as described in Section 2.1.1. A base board was also design so the stator could be mounted on. A layer of conductive adhesive was applied between the stator and the piezoelectric tube.

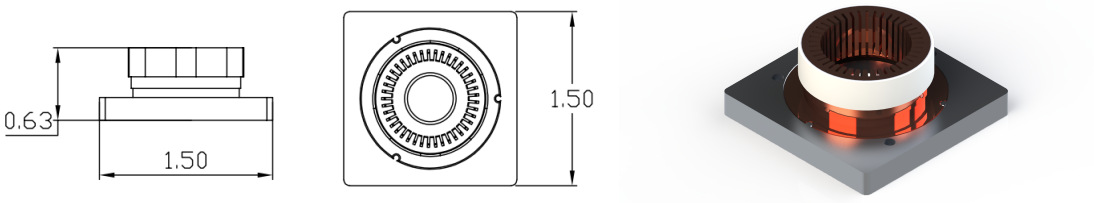


(a) Assembly Dimension (inch) (b) Assembly Render

Figure 2.3: Stator Assembly

### 2.1.1 Piezoelectric Tube

Through our previous simulation results, we noticed when changing the height of the piezoelectric tube, the deformation zone on the stator stayed almost the same. Fig. 2.5 shows the comparison how the motion differs when the height of the tube is changed at 1/2" and 1/4". The piezoelectric tube with 1" outer diameter at the

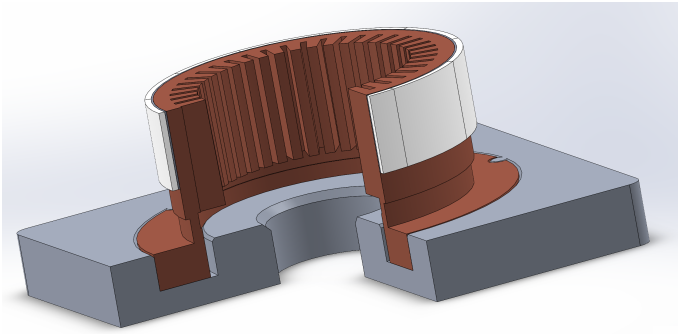

Figure 2.4: Stator Assembly Cutaway View

height of 1/2" was taken into consideration by using a FEM simulation to research on the deformation of the stator while driving by two 90° shifted sine waves. Fig. 2.5(a) indicates only the deformation generated by the top section of the piezoelectric tube has been transferred to the stator. In that case, we simulated the motion of another piezoelectric tube at 1/4" height. According to the simulation result of both setting ups, the 1/4" height of piezoelectric tube was selected.

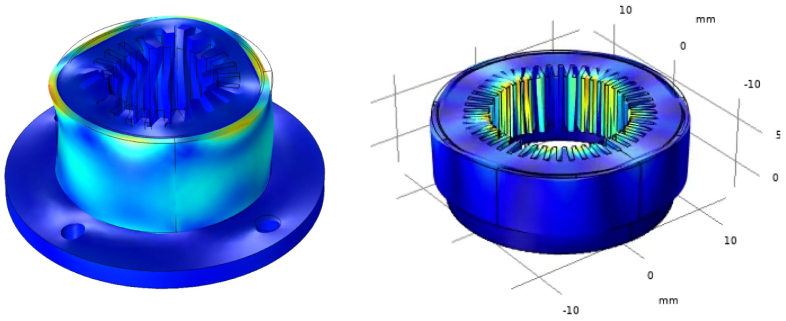


(a) Tube Height at 1/2" (b) Tube Height at 1/4"

Figure 2.5: Previous Simulation on Height of the Tube

Mimicking the properties of the piezoelectric ring that using on the commercially available USR30 motor(Shinsei Corporation, Japan), the thickness of the tube's was set to 0.02". The outer diameter of the tube was set to be 1". Fig. 2.6 shows the dimension and render of the piezoelectric tube.

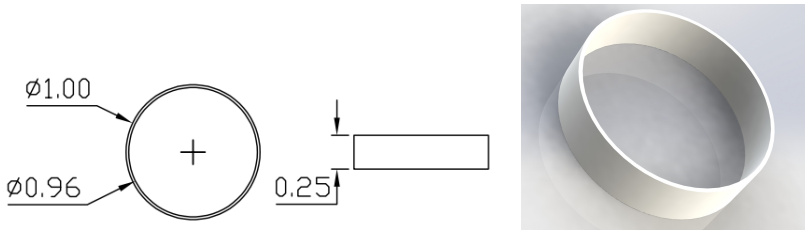


(a) Dimension of Piezoelectric Tube (inch) (b) Render of Piezoelectric Tube

Figure 2.6: Dimension and Render of Piezoelectric Tube

### 2.1.2 Stator

A stator at the size of 0.95" (diameter) × 0.34" (height) was designed on a flange at the size of 1.2" (diameter)×0.12" (height) , shown in Fig. 2.7. Forty-one notches were evenly distributed on the inner surface of the hollow area to increase the flexibility of the stator. Each notch was designed as 2.5mm (height)×0.76mm (width), the gap between the notches was 0.5mm, and the thickness of the wall was 1.5mm. Changing the dimensions for the notches will change the flexibility and the size of contacting area, which will make influence on transiting the traveling waveform from the piezoelectric ring to the rotor. Gaps was designed on both inner and outer side of the tube to reduce the constrain from the flange. Three pilots holes were made around the flange outer surface as a reference for assembling.

In order to test the difference between line contact and surface contact, the notches were tapered by 1° from the bottom, which left the minimum diameter of the hollow hole to 0.66". The render of the stator can be seen in Fig. 2.8.

### 2.1.3 Base Plate

A base plate was designed as a mounting method for the stator. A 0.12" depth slot was made on the top surface of the base plate to fit the whole flange in. Three

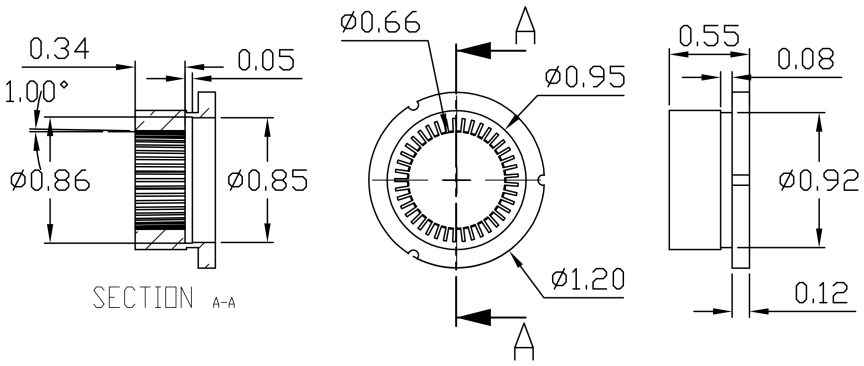


Figure 2.7: Dimension of the Stator (inch)

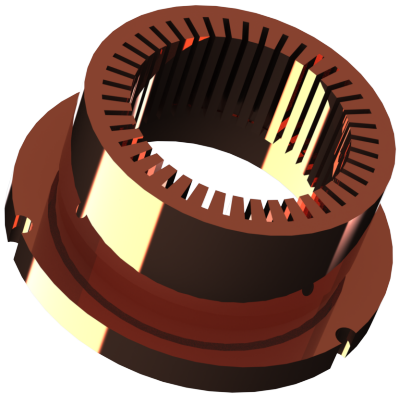

Figure 2.8: Render of Stator

align keys along the side of the slot were used to guide the direction of the stator. A hole in 0.4" diameter was designated for penetrating the effector. The detailed dimension and render of the base plate is shown in Fig. 2.9.

## 2.2 Material Selection

PZT-5H is the material we choose for the piezoelectric tube. According to the table of characteristics of different piezoelectric tubes that we obtained from EBL Products, Inc., EBL #3 which is using PZT-5H has the highest amplitude among all the

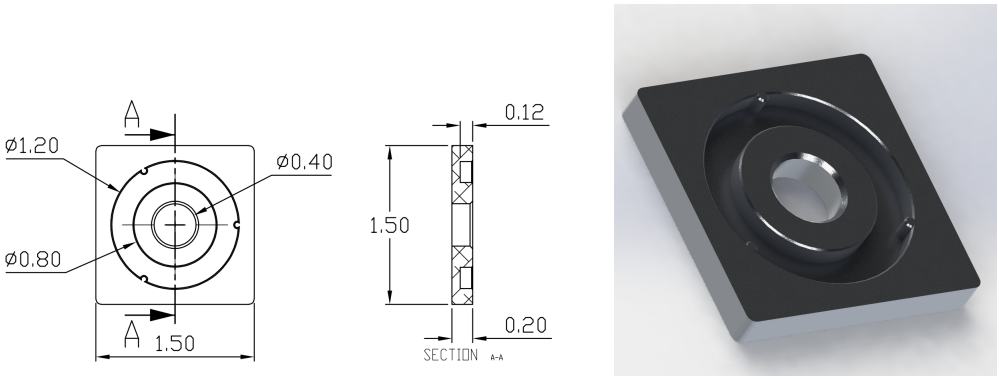


(a) Dimension of Base Plate (inch) (b) Render of Base Plate

Figure 2.9: Base Plate

other materials that can be easily obtained, when comparing under same conditions. The characteristic of PZT-5H is marked in a red rectangular in Fig. 2.10. [37] Although the amplitude and other key performance parameters of material EBL #23 are better than what PZT-5H has, that kind of material is just a tester which is not marketed yet. Thus, PZT-5H has been proved functional as other researchers at A.I.M. lab has already used it for years.

| MATERIAL PROPERTIES | EBL #1 | EBL #2 | EBL #3 | EBL #4 | EBL #9 | EBL #23 | EBL #25 |
|---|---|---|---|---|---|---|---|
| $d_{31}$Å/V@293°K | -1.27 | -1.73 | -2.62 | -.95 | -1.35 | -3.20 | -1.90 |
| $d_{33}$Å/V@293°K | 2.95 | 3.80 | 5.83 | 2.20 | 3.15 | 6.50 | 3.90 |
| $d_{31}$Å/V@4.2°K | - | -0.31 | -0.33 | - | - | - | - |
| $d_{33}$Å/V@4.2°K | - | 0.69 | 0.74 | - | - | - | - |
| Dielectric constant $K_3^T$ | 1300 | 1725 | 3450 | 1050 | 1450 | 3800 | 1800 |
| AC depoling field kV/cm rms | 10 | 7 | 4 | 15 | 10 | 5 | 7 |
| Young's modulus $10^{10}$ N/m$^2$ | 8.1 | 6.3 | 6.3 | 8.5 | 7.5 | 7.5 | 7.9 |
| Curie Temperature °C | 320 | 350 | 190 | 300 | 320 | 250 | 350 |
| Thermal conductivity W/m°C | 2.1 | 1.5 | 1.5 | 2.1 | 2.1 | 2.0 | 2.0 |
| Thermal expansion coefficient ppm/°C | - | - | 4.7 | 3.0 | - | 3.5 | 3.0 |
| Density g/cm$^3$ | 7.5 | 7.5 | 7.45 | 7.5 | 7.6 | 7.8 | 7.7 |
| Mechanical Q | 400 | 100 | 65 | 960 | 600 | 30 | 80 |
| Poisson's ratio | 0.31 | 0.31 | 0.31 | 0.31 | 0.31 | 0.31 | 0.34 |
| Industry type | PZT-4 | PZT-5A | PZT-5H | PZT-8 | PZT-4D | - | - |

Figure 2.10: Characteristic of Different Piezoelectric Tubes

Since the future goal for this project is the application within a high magnetic field, i.e., inside MRI scanner, a layer of copper was applied on the inner and outer surface of the piezoelectric tube. The electroless copper layer was used as the electrode for PZT-5H because of its nonferromagnetic properties.

The stator was manufactured using brass C360. As an alloy that contains copper and zinc, brass is also nonferromagnetic and has a good thermal conductivity, which makes it a favorable substitute material for copper. It maintains the flexibility of copper, and also easier to be manufactured than copper. From the material guide from Protolabs, Inc., brass C360 is the only material that can be processed with CNC turning, as the marked section shown in Fig. 2.11. [38] Thus, brass is also widely used to manufacture the stator in the commercial ultrasonic actuators produced by Shinsei Corporation, Japan.

| Type | Material | Service | Process | More Info |
|---|---|---|---|---|
| Brass | Brass C260 | Sheet Metal Fabrication<br>CNC Machining | Sheet Metal Fabrication<br>CNC Milling | Data Sheet (Sheet Metal)<br>Data Sheet (CNC Milling) |
| Brass | Brass C360 | CNC Machining | CNC Turning | Data Sheet |
| Copper | Copper C101 | Sheet Metal Fabrication<br>CNC Machining | Sheet Metal Fabrication<br>CNC Milling | Data Sheet (Sheet Metal)<br>Data Sheet (CNC Milling) |

Figure 2.11: Material Selection Guide from Protolabs, Inc.

Since the actuator we are building was using friction coupling method, a higher friction force is desired for a better motion transmission ability.

$$f = \mu \times N \tag{2.1}$$

Considering the same normal force $N$ is provided, the raise of coefficient of friction $\mu$ will also increase the friction force $f$ in Eq. 2.1. The coefficient of friction between

two copper surfaces is normally 0.17, whereas the coefficient of friction between aluminum and copper is around 0.27. Aluminum possess one of the highest coefficient of friction among the nonferromagnetic materials, and it is easier to be manufactured than others, for example, crystals and plastics.
All of the material's properties mentioned above are provided in Appendix A.

## 2.3 Manufacturing

Since the piezoelectric tubes that we used were purchased before the simulation which compared the impacts that different height of piezoelectric tube would bring, the tubes that in our stock were all at 1/2" height. In order to reduce the unnecessary cost, we decided to cut the tubes into half. A holder was built first to prevent undesired movements while cutting the piezoelectric tube.
With the piezoelectric tube fasten on, the holder was put on a lathe. A pneumatic die grinder with a tiny diamond blade was used as the cutter. Fig. 2.12 shows the configuration of the cutting process. Around 0.018" height of material was lost during the cutting process.

After cutting the tubes into 1/4", the electrode surface was etched to isolate the segments, following the pattern shown in Section 3.2. Details of etching process is shown in Appendix C.
The stator was manufactured by Protolabs, Inc. using lathe and wired EDM. Due to the limitation of the machining technique, a 0.007" radius was left on the bottom of each notch.
The base board was 3d printed using carbon fiber with MarkForged Mark Two 3D printer. Mounting holes were tapped so that the stator can be fastened on with

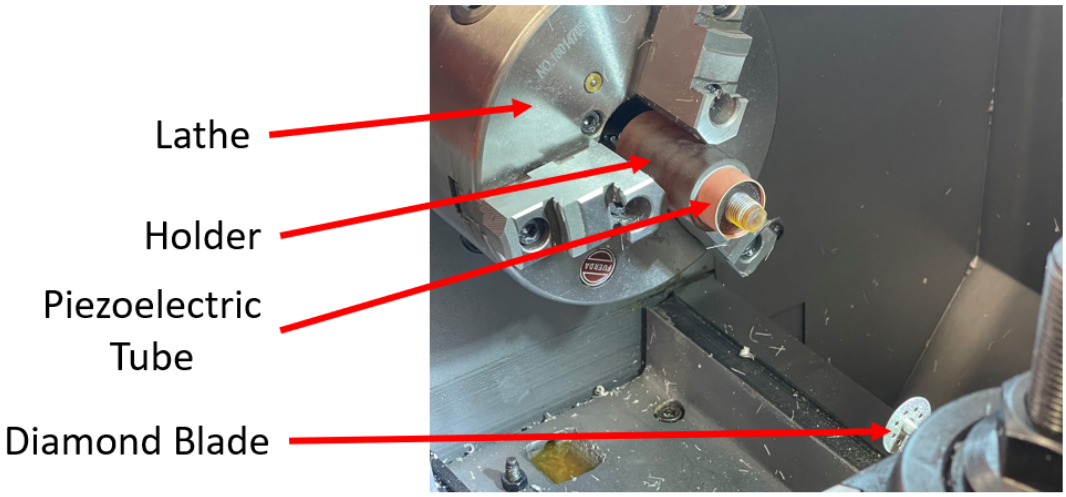


Figure 2.12: Piezoelectric Cutting Setup

#4-40 screws and washers.

Three rotors were manufactured using lathe following the dimensions described in Section 4.1.1.

The complete assembly of the stator is shown in Fig. 2.3, which includes the base board, piezoelectric ring, conductive adhesive ring, and the stator.

# Chapter 3

# FEM SIMULATION AND RESULTS

Finite element method (FEM) was used to simulate the deformation of our hollow cylindrical motor assembly. COMSOL Multiphysics® 5.5a (COMSOL) was used to configure the material properties of the elements imported from SolidWorks, generate multi-physics relationship between each element. Studies on the designated multi-physics relationship were also solved in COMSOL, following the instruction of [39].

## 3.1 Simulation Workspace Setup

In a default COMSOL workspace set up, the local coordinate system is oriented along the global rectangular coordinate system according to right-hand rule. In order to represent the traversal and orientation of a hollow cylindrical model as shown in Fig. 3.1, a group of local cylindrical coordinates was set and represented with the local coordinate system as shown in Table 3.1. [40]

| Local Axis | Cylindrical Coordinates |
|---|---|
| x1 | $\Phi$ (Azimuthal) |
| x2 | $z$ (Axial) |
| x3 | $r$ (Radial) |

Table 3.1: Relation between Local Cylindrical Coordinate System and COMSOL Default Local Coordinate System

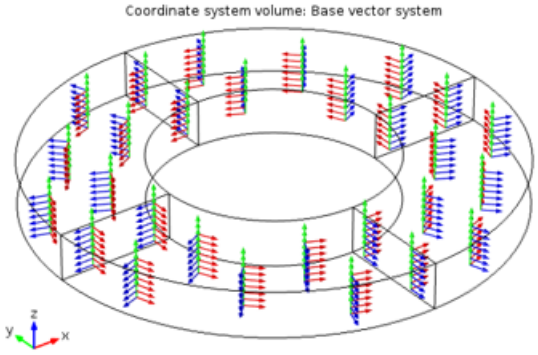


Figure 3.1: Desired Cylindrical System w.r.t. Base Frame

A unit vector can be expressed as[1]

$$\hat{e} = a\hat{X} + b\hat{Y} + c\hat{Z} \tag{3.1}$$

where $\sqrt{a^2 + b^2 + c^2} = 1$.

$$\hat{e}_\phi = -sin\phi\hat{X} + cos\phi\hat{Y} + 0\hat{Z} \tag{3.2}$$

$$\hat{e}_z = 0\hat{X} + 0\hat{Y} + 1\hat{Z} \tag{3.3}$$

[1]X,Y,Z in COMSOL setting represents the material frame instead of global frame.

$$\hat{e}_r = cos\phi\hat{X} + sin\phi\hat{Y} + 0\hat{Z} \tag{3.4}$$

A local cylindrical coordinate system was defined to model radial polarization of the piezoelectric tube. The voltage across the piezoelectric tube and the radial polarization of the material are shown in Fig. 3.2. The elements would be shorted together with each adjacent segment polarized in an opposite direction.

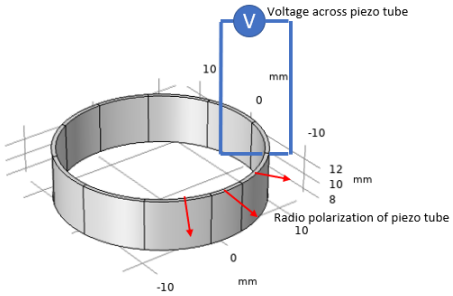


Figure 3.2: Voltage Across Piezo Tube

According to the desired polarization generated by the voltage cross the piezoelectric tube, we set the cylindrical coordinated directions that corresponded to to the local coordinates as shown in Table 3.2.

| | x | y | z |
|---|---|---|---|
| x1 | -sin(atan2(Y,X)) | cos(atan2(Y,X)) | 0 |
| x2 | 0 | 0 | 1 |
| x3 | cos(atan2(Y,X)) | sin(atan2(Y,X)) | 0 |

Table 3.2: Cylindrical Coordinate System Corresponding to Global Rectangular Coordinate System

## 3.2 Methodology

As the main purpose of the simulation was to simulate the deformation of the stator on the notches, the baseboard, the cover, and the rotor were temporarily removed, only left the assembly of stator, conductive adhesive and piezoelectric tube in the CAD model. The assembly was imported from SolidWorks through COMSOL's CAD kernel. The model was first orientated and traversed to match the default coordinate system of COMSOL, with the bottom surface attached to the XY-plane and center of mass (COM) of the surface located at origin point which was $(0, 0, 0)$, as shown in Fig. 3.3.

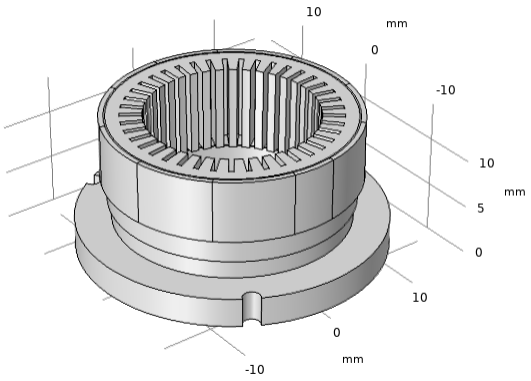


Figure 3.3: Stator Assembly Imported from SolidWorks

A union was created automatically because the all components of the assembly are adhered together, which means none of them will move with respect to one another. A virtual operation called ignore edges was used to remove redundant edges to avoid meshing issues.

Domains were assigned with different material according to the material selection Section 2.2. Material properties were mostly defined by COMSOL with respect to

the temperature and other relevant issue that may impact on the performance of the material. However, some of the material properties were not provided by COMSOL, so we searched online to fill in the required fields. The basic material properties can be observed in Appendix A.

A piezoelectric effect multiphysics module was add to the import geometry. The module brought in the electrostatics and solid mechanics physics modules.

The solid mechanics module was setup to take all components of the assembly in to the coming studies. The piezoelectric tube was set as a piezoelectric material and the remaining components including the conductive adhesive and stator were considered as linear elastic materials. The fixed constrain was set on the bottom surface of the stator since three screws would be installed to hold the stator on the base plate. All the components were using global vector system except the piezoelectric tube. In the piezoelectric section, the coordinate system was set to be the frame that we mentioned in Section 3.1.

Probe is a node in COMSOL that allows user to monitor the development of a scalar quantity from a time-dependent study. [41] Three boundary probes were set on the surface of one of the notches at three different section as shown in Fig. 3.4. Probe #1 was put on the top section of the notch, which was the edge that shared with the top surface of the stator, at $(5.1519, 6.789, 13.882)$. Probe #2 was put on the middle section of the notch, at $(5.0876, 6.7834, 11.387)$. Probe #3 was put on the bottom section of the notch, which was the edge that shared with the bottom surface of the notch, at $(5.0714, 6.6622, 5.286)$.[2] The boundary probes were configured to collect the displacement of the notch on the x-y plane to observe and compute a few parameters of the motor including the settling time.

[2]All the probe locations mention are with respect to the spatial frame and unit is $mm$.

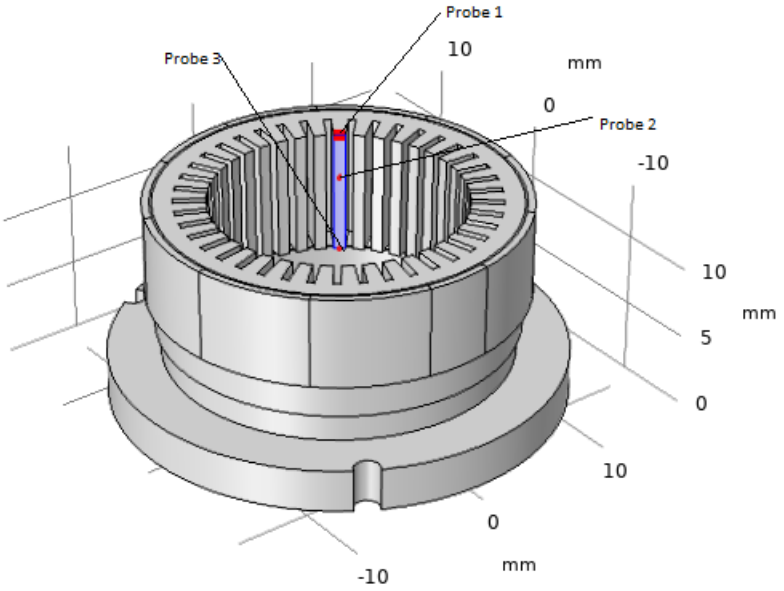


Figure 3.4: Probe Setup on the Stator

The electrostatics module was setup only on the piezoelectric tube. The tube was separated to eleven individual elements. The electrical connection of each piezoelectric element was following the pattern shown in Fig. 3.5, which has been proved to work in the previous research on plastic piezoelectric actuator presented in [32]. The inner-side of the piezoelectric tube which shared a boundary with the conductive adhesive, was set up as ground as the green circle in the figure. Segment 1, 10 and 11 were left as free charge area. Segment 2-9 were assigned to four electrical potentials groups. In the figure, green circle represents ground, red lines represent positive signal input, blue lines represent negative signal input, and white represents isolation and zero charge areas.

The electric potential were in the form of Equation 3.5, as a variable dominated by time. In the equation, $A$ was the controller of the sign, $V_i$ was the driving voltage, $freq_i$ was the selected frequency for simulation, and $t$ was the time collected by solver.

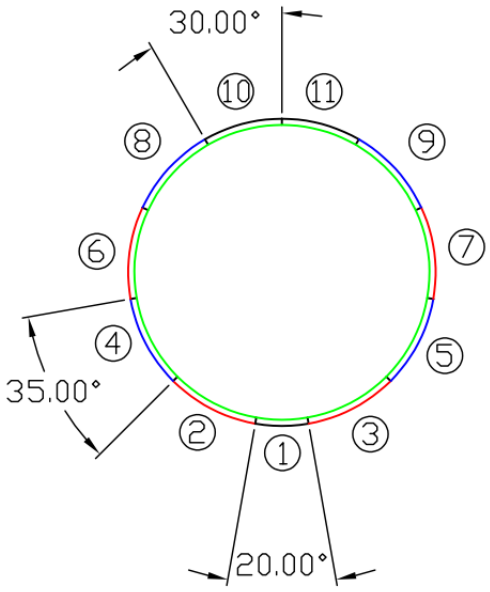


Figure 3.5: Pattern on Piezoelectric Tube

$$A \times V \times sin(2 \times \pi \times freq_i \times t + \phi) \tag{3.5}$$

In our simulation, the group of input signals contained a positive sine wave, a negative sine wave, a positive cosine wave, and a negative cosine wave. Fig. 3.6 shows the connection to corresponding electrodes. A formal description of the waveform is provided in [42]. The negative of $A$ provided a negative wave. In order to act a phase shift, a $\phi$ of $\pi/2$ was used to represent the cosine domain. The driving voltage $V$ was set at 60V throughout the whole simulation process.

In order to balance the processing time and result accuracy of a FEM simulation, an appropriate meshing setup is of great importance. The meshing parameters in

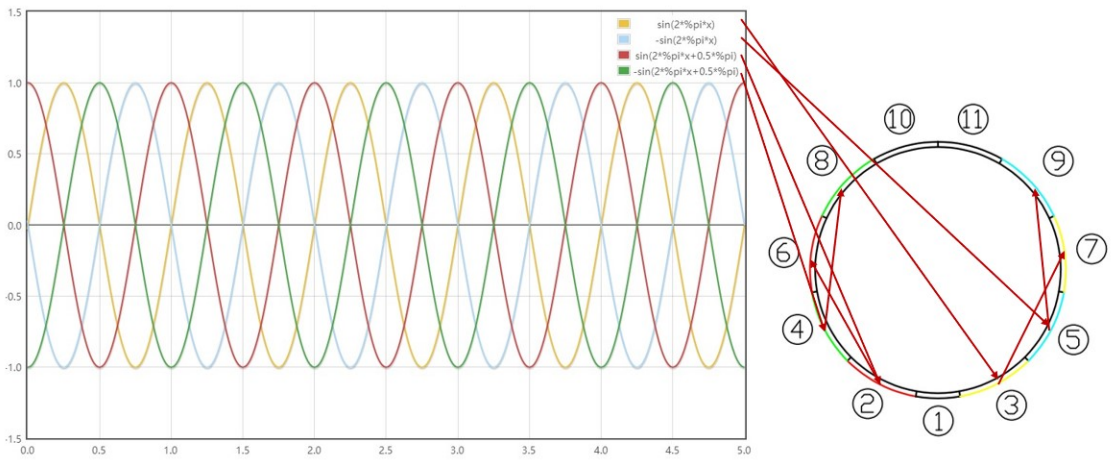


Figure 3.6: Phase Corresponding to Electrodes

our simulation are shown in Table 3.3. A finer meshing setting was supposed to be selected due to the existence of small mounting hole on the bottom of the stator. However, since there would be no motion on that portion of stator as it was a plate which had a parallel surface set as fixed constrain, a coarse method was finally selected to enhance simulation performance. One warning was shown up because of the issue mentioned above, however, it would not affect the result of simulation. The meshing result is shown in Fig. 3.7.

| | |
|---|---|
| Max Element Size | 4.57 |
| Min Element Size | 0.853 |
| Max Element Growth Rate | 1.6 |
| Curvature Factor | 0.7 |
| Resolution of Narrow Regions | 0.4 |

Table 3.3: Meshing Properties for Stator Assembly

An eigen frequency study was added to the model to determine the resonant modes of the stator and at which frequencies that the modes will happen. The theory for this study is the solver assumes the stator will run at a certain eigen frequency, and it will come up with the shape corresponded to the mode. The main purpose

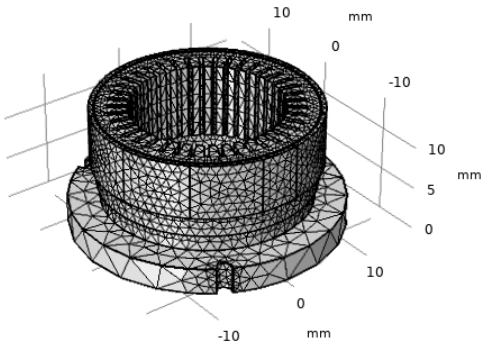


Figure 3.7: Mesh Results of the Assembly

of eigen frequency study is to help us find out the certain frequencies that we can drive the motor, which was only about the physics of solid mechanics. In that case, electrostatics and multiphysics coupling nodes were unchecked. In our simulation, the frequencies were searched around 30 kHz for 20 modes.

After receiving the frequencies for each mode, a time dependent study node was add to the assembly. The time range of this study is set to be

$$range(T_0, 1000/freq_i/100, T_{end}) \tag{3.6}$$

when considering the motion at a certain driving frequency at $freq_i$. In Eq. 3.6, $T_0$ and $T_1$ represents the starting and ending time for the time domain study. The parameter $1000/freq_i/100$ represents the time lapse for each frame.

## 3.3 Result

### 3.3.1 Eigen Frequency

The result of eigen frequency are presented in Table 3.4. Due to the first excitation mode could not be considered as a stable mode, the eigen frequency study in

COMSOL was not able to calculate the frequency at the first mode. The excitation frequencies for each mode is shown in Table 3.4.

| Mode Number | Frequency (kHz) |
|---|---|
| 2 | 12.242 |
| 3 | 14.658 |
| 4 | 21.520 |
| 5 | 30.031 |
| 6 | 39.181 |

Table 3.4: Eigen Frequency Result for Each Mode

The shapes of different modes are shown in Fig. 3.8 and Fig. 3.9. The figures were scaled up by 54000.66394 since the deformation of the stator was too tiny to be identified. The maximum deformation would be around $4.5 \times 10^{-6}$ mm.

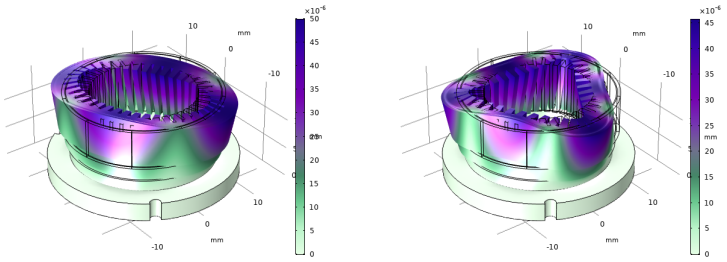

(a) Mode 2 at 12.242 kHz (b) Mode 3 at 14.658 kHz

Figure 3.8: Stator Shapes at Mode 2, and 3

According to our previous research on the plastic piezoelectric motor, the motor would reach an excited state that the rotor could rotate constantly. [32] In that case, the simulation on the motion of the stator was based on the fifth mode. The excitation frequency of the fifth mode was 30.031 kHz, which fall in the range that our high voltage supply could provide.

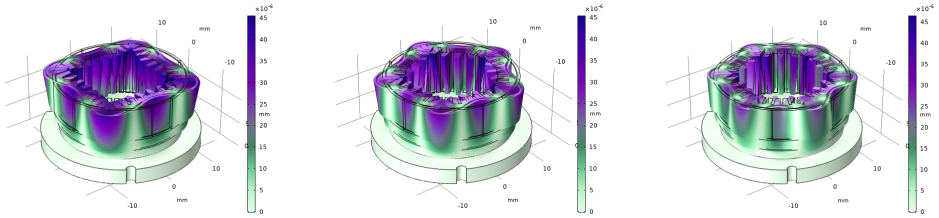

(a) Mode 4 at 21.520 kHz (b) Mode 5 at 30.031 kHz (c) Mode 6 at 39.181 kHz

Figure 3.9: Stator Shape at Mode 4, 5, and 6

### 3.3.2 Setup 1

The first setup was following the methodology mentioned in Section 3.2. Fig. 3.10 shows the displacement of the specific notch which we put the boundary probes on based on time domain simulation. The three lines represented the three probes we set. The blue line was the probe at the top surface of the notch which has the largest displacement among the three areas. The green line was the probe at middle of the notch, where the amplitude was slightly lower than the deformation at the top surface. The red line represented the probe at the bottom of notch, which was not covered by the piezoelectric tube at all. The amplitude decreased in order from the top surface to the bottom. The center lines of the three sine amplitude share the same period.

The stator reached the first peak at around 0.2 ms, where the notches reached the first largest displacement. The duration for each period which contained two peaks was around 0.4 ms. However, it may not be qualified as settled because the amplitude of the sine wave was on a decreasing trend. Future work will be required to identify the settling state for this motor.

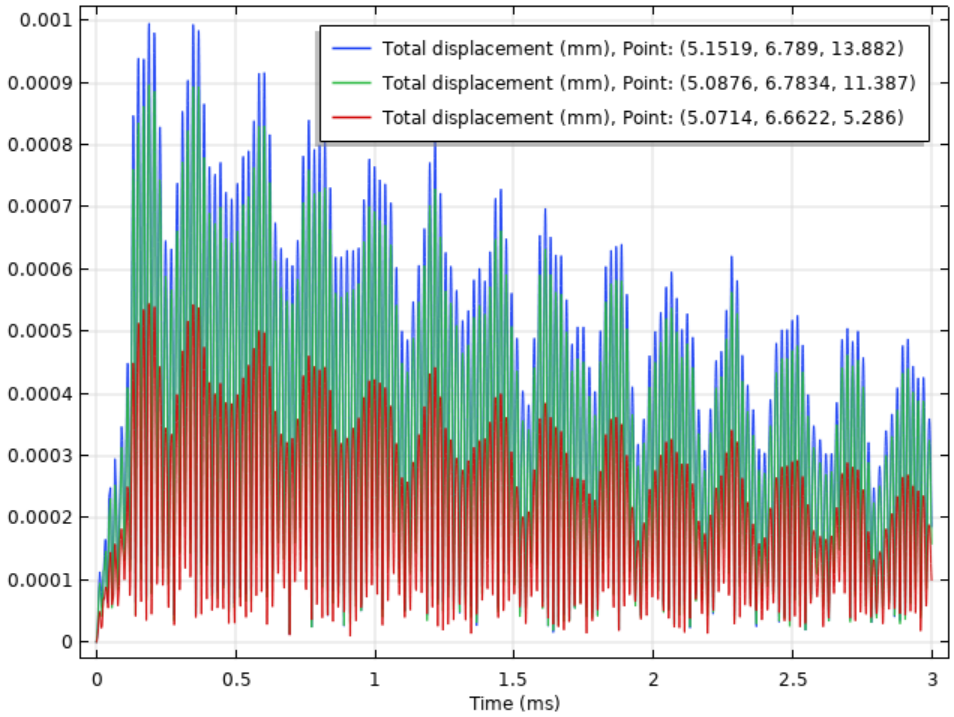


Figure 3.10: Displacement of the Notch (mm)

### 3.3.3 Setup 2

The second setup was to switch the electrode assignment between the negative sine wave and the negative cosine wave as shown in Fig. 3.11. The wave that electrode #5 and #9 connected to were switched from negative sine wave to negative cosine wave, and the negative cosine wave that connected to electrode #4 and #8 were replaced with negative sine wave.

Fig. 3.12 shows the displacement monitored by the probes on the notch. It took around 0.75 ms to reach the first peak of the sine amplitude wave, and the duration for each period was around 2 ms.

From Fig. 3.12, we also found the amplitude of the sine wave was on a decreasing

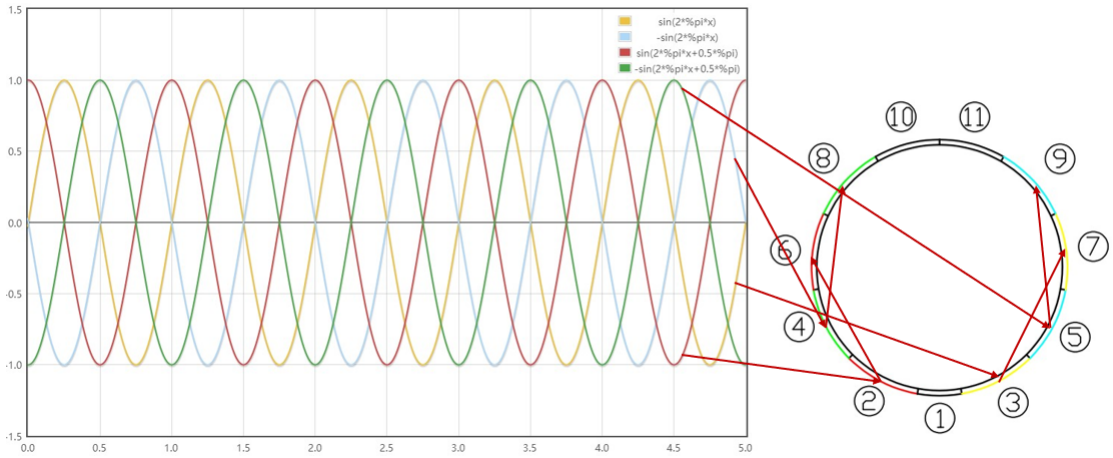


Figure 3.11: Electrode Signal Setup for Setup 2

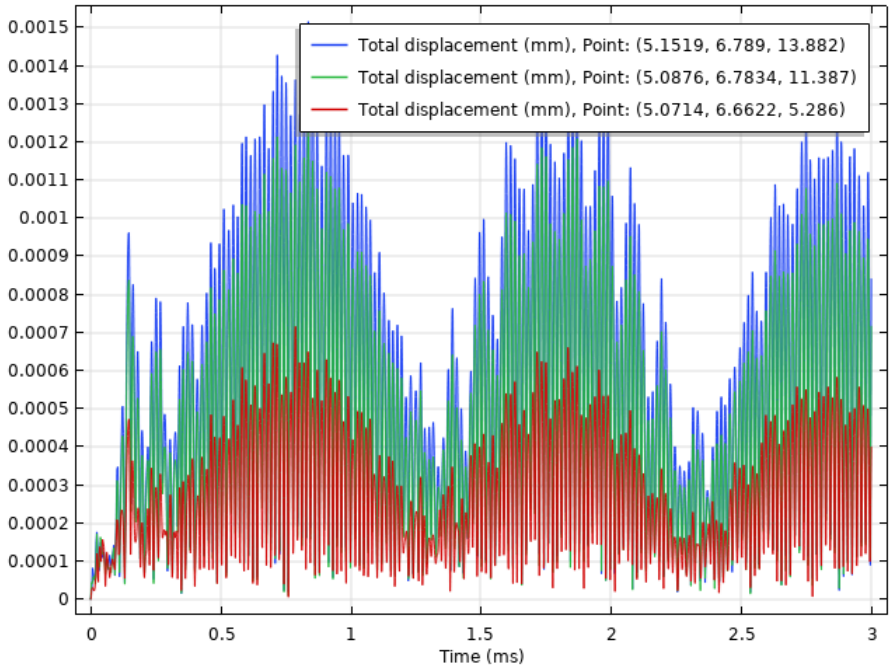


Figure 3.12: Displacement of the Notch after Phase Assignment Switching (mm)

trend.

### 3.3.4 Setup 3

The third setup was adding a fixed constraint to the top surface of the epoxy in order to eliminate the motion on the z-axis while the piezoelectric tube was at excitation state. With the constraint placed, the eigen frequency study was used again to check if there was any impact on the excitation frequencies for each drive mode.

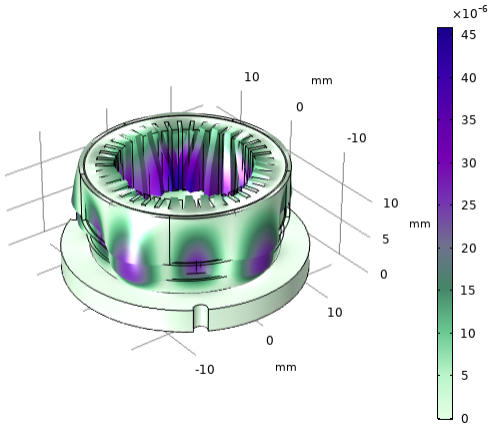


Figure 3.13: Mode 5 Shape with Top Constrain at 41.381 kHz

The simulation showed the updated model would be able to reach the fifth mode at 41.381 kHz with a maximum deformation below $45 \times 10^{-6}$ mm, where it contained five peaks on the inner face of the stator. Fig. 3.13 shows the shape of fifth mode when the constraint was placed, in which only the lower section of the notches can be actuated.

Fig. 3.14 shows the displacement monitored by the probes. Although the displacement with respect to time was still following the pattern of a sine wave, it was hard to identify the either the amplitude or the period. The highest amplitude occurred

on the bottom section of the stator, which was represented with the red line at around $70 \times 10^{-5}$ mm. Due to the fixed constraint configured on the top of the layer of epoxy, the displacements of the top surface and middle section were incredibly small comparing with the bottom surface.

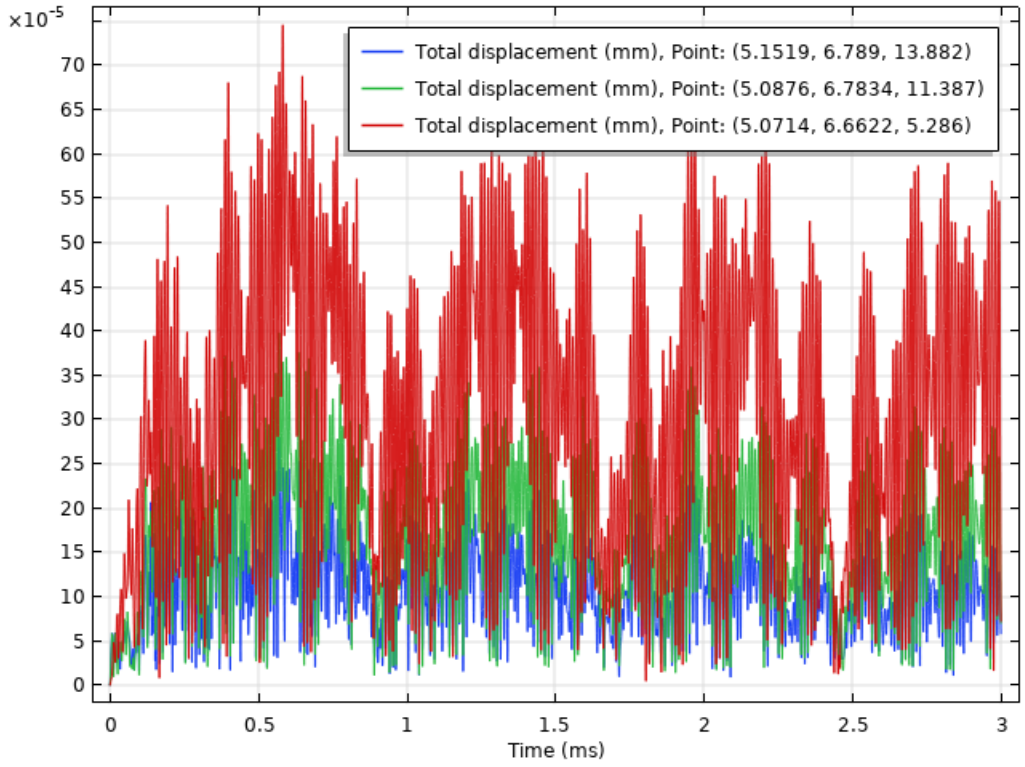


Figure 3.14: Displacement of the Notch (mm)

## 3.4 Comparison

Comparing between setup 1 and setup 2, when changing the electrode segments position, the period of the sine wave representing the amplitude of stator was extended to around four times of the original duration, however, the peak of displacement was not differed much. The result of comparison matched our assumption, due to a normal negative cosine wave is always a full quarter of period ahead of the negative sine

wave. No matter which phase was provided to the notch that we are monitoring, when the displacement on it was decreasing, i.e. the wave is switching to negative portion, the closest segment of piezoelectric will prevent the trend because its displacement increasing at the same time.

The tendency that the amplitude were decreasing showed up in all three setups, and it was not able to keep at the same amplitude as we mentioned as settle state, which is different from the previous research on the planar rotary piezoelectric motor in [39]. The assumption on this phenomenon was since the stator was providing a vibration to the rotor for a spinning motion, the stator itself may also possessed a motion like a cam rotating inside.

# Chapter 4

# REAL WORLD VALIDATION AND RESULTS

In order to validate the design in real world, we manufactured the parts and assembled them together following the original motor design, as we presented in Section 2.3. Fig. 4.1 shows the completely assembled stator. A driver system was set up to test the motion appearance of the actuator at different voltages, frequencies and preloads.

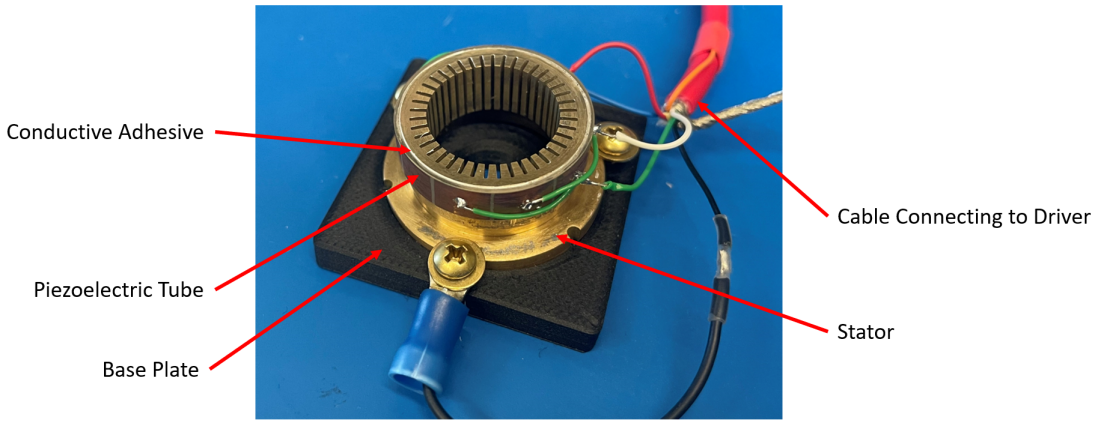


Figure 4.1: Assembled Stator

## 4.1 Test Space Setup

### 4.1.1 Hollow Cylindrical Motor Setup

According to our simulation result, as shown in Fig. 3.10, the displacement on the notches decreased in the order from the top surface to the bottom. In order to test the impact that caused by the contacting method, three shafts that with different geometries properties were used for comparison as shown in Table 4.1. Shaft #1 was based on the face contacting method with 1° tapered. Shaft #2 and #3 were based on line contacting method. The location of contacting line on the stator between the stator and the rotor varies due to the diameter change of shaft #2 and #3. Fig. 4.2 shows the three shafts' appearances.

| Shaft Number | Height | Diameter | Angle | Weight |
|---|---|---|---|---|
| 1 | 6.35 mm | 16.84 mm (Minimum) | 1° | 5.34 g |
| 2 | 2.54 mm | 16.90 mm | 0° | 2.41 g |
| 3 | 2.22 mm | 17.00 mm | 0° | 2.52 g |

Table 4.1: Shaft Configurations

(a) Shaft #1 (b) Shaft #2 (c) Shaft #3

Figure 4.2: Shafts

Fig. 4.3 indicated the contacting area when the rotors are installed on the stator. The green lines represented the desired area for contacting on the notches. Rotor #1 in Fig. 4.2(a) was supposed to contact all the top surfaces of the notches that

covered by the piezoelectric tube, and establish a steady face contact. Rotor #2 and #3 were contacting the bottom half and top half sections where it is covered with the piezoelectric tube.

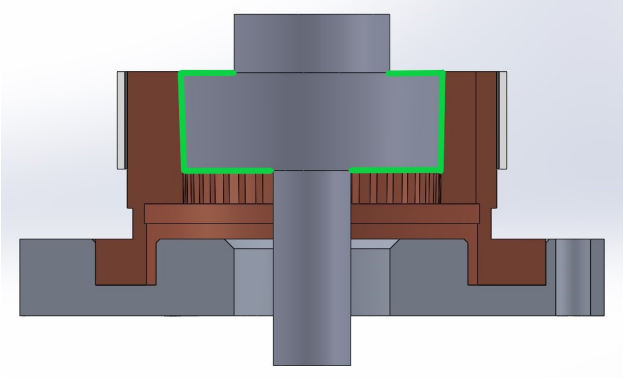

(a) Rotor #1 Contacting Model

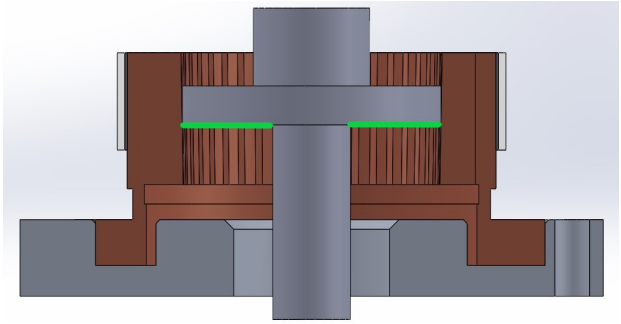

(b) Rotor #2 Contacting Model

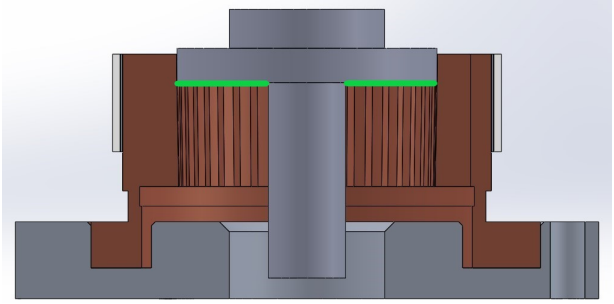

(c) Rotor #3 Contacting Model

Figure 4.3: Contacting Model for Each Rotor

Two stator assemblies was built up for comparison.

### 4.1.2 Driver Setup

A high voltage power supply system developed by Dr. Nycz, Dr. Carvalho, and Dr. Gandomi was used to excite the actuator. A Rigol waveform function generator (DG1022Z) was used to create two 180° shifted sine wave signals. The cosine waves were created by shifting the previous sine wave signals by 90°. The resulting 4 wave signals were amplified through PA94 operational amplifiers from Apex Microtechnology, and set to an inverting configuration powered from a pair of RC125-0.3P and RC125-0.3N 300V power supplies from Matsusada. The amplified ratio of the power supply is 1:100. The driver system is shown in Fig. 4.4. The motor was connected to the driver system with a 6-pin molex connector.

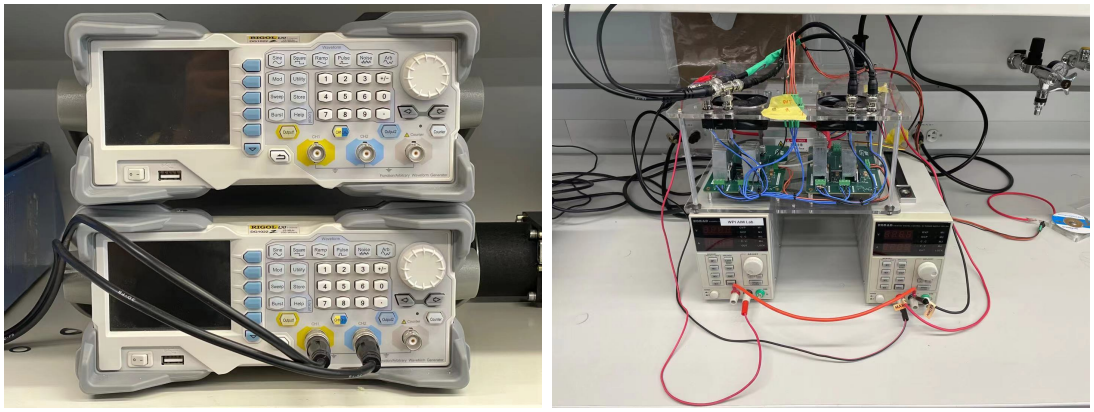

(a) Function Generator (b) Power Supply System

Figure 4.4: Driver System Setup

## 4.2 Methodology

The stator assembly was connected with the driver system presented in Section 4.1.2. Holography was the first method that came to our mind. Holography is using diffraction to reproduce the image of the original scene with depth and other pa-

rameters. [43] Instead of forming an image by lens, a holography is a recording of the light field of the object. It needs a laser light to brighten the object and view the results. [44] A holographic image can represent the displacement in the vertical direction of a surface, which has been proved to work in [33]. However, due to the structure of our stator design and the simulation results, the desired motion will not make any change in height on the top surface of the stator, which is undesired for holography. In that case, we was not able to identify the driving mode using holography. Thus, as we presented in Section 3.3, the change of the stator was too small to be observed even with a high speed camera. There is another noticeable phenomenon when the stator is in a driving mode, which is the noise of vibration. In this thesis, due to the limit of experiment equipment, we will use both the noise and the motion of rotors to validate the model.

The deformation of the stator assembly was first tested. The frequency was first set to be 11.992 kHz on the waveform function generator, which was 50 Hz lower than the second driving frequency that we received from the simulation. The amplitude was set to be 600 $mV_{p-p}$ which will trigger the high voltage power supply to provide a voltage at 60 V. The stator assembly was excited without putting the rotors on. The frequency was increased by 10 Hz every step till we can hear a clear and constant high frequency noise. Then we increased the frequency within a range of 500 Hz from the frequency that the first noise occurred to find the frequency that generated the loudest noise. The frequencies were recorded for motion validation. Same steps were repeated to validate other frequencies from the simulation results around the other driving modes shown in Fig. 3.4. However, the frequency for the sixth mode, which is around 39.181 kHz, was too high for our auditory system to catch.

With the approximate frequency found for each driving mode, we disconnected the power to the stator assembly to shrink the heat that built up during the driving

mode locating process. A GoPro was used to record the motion during the validation. After cooling the stator back to room temperature, we changed the frequency back to the first mode we found for the specific stator, and powered it on. Rotor #1 was carefully put into the center of the stator to see if the rotor could be actuated. Our simulation was based on the stator assembly itself only, which means it did not require a high gain to excite the motion because no preload was applied. With the rotor putting on, a preload was initialized and applied to the stator, which means a high gain would be required to bring the rotor into life. The gain was controlled by the amplitude of the power provided by the high voltage power supply, which was controlled by the amplitude of signal from the waveform generator. The amplitude of the waveform generator was changed within the range between 600 $mV_{p-p}$ and 1.5 V, with 100 $mV_{p-p}$ for each step. If the rotor could be excited, the frequency was adjusted within $\pm$ 300 Hz to find at which point the rotor could rotate at a constant condition. If not, we reset the amplitude to 600 $mV_{p-p}$ and proceed to the frequency of next driving mode.

Once the stator was able to rotate constantly, the rest of the rotors were placed on the rotor as weights to increase the preload. All the motion of the stator and the parameters of setting up were recorded. A mark was put on the top surface of each rotor to observe the motion. The same steps were repeated for rotor #2 and #3.

## 4.3 Result

The excitation frequencies for each mode were identified by the resonance noise that were generated while applying the voltage to the electrodes as we mentioned in Section 4.2. Table 4.2 shows the approximate excitation frequencies for each mode.

| Mode Number | Excitation Frequency (kHz) | |
|---|---|---|
| | Motor 1 | Motor 2 |
| 2 | 12.296 | 12.122 |
| 3 | 14.576 | 14.202 |
| 4 | 21.496 | 21.622 |
| 5 | 30.822 | 30.622 |

Table 4.2: Driving Frequencies Identified by Resonance Noise

The sixth mode which was supposed to be around 39.181 kHz, was too high to be captured by human's auditory system. We were able to notice a noise was existing, however, it was unable to identify at any specific frequency where the stator reached its peak performance. In that case, we only listed the excitation frequencies from the second to the fifth mode in this section.

The manufacturing tolerance has made rotor #1 too small to fit and stayed at the desired position while coupling with the stator. A layer of Teflon® TPFE tape was put on the tapered surface to increase the size of the rotor to keep it stays at the desired location, mimicking the Teflon® TPFE layer that Shinsei Corporation put between the stator and rotor on their commercial products. Vibration of the stator was noticeable because of the noise, however, the rotor could not be actuated at any frequencies with any amplitude. The same circumstances happened when we replaced the TPFE tape to copper tape.

Rotor #2 was able to fit in the stator, however, the contacting zone was a little bit lower than where we expected in Fig. 4.2(b). No motion was generated while adjusting the frequencies around the second mode which was 12.296 kHz. When we changed the frequency to the third mode which was at 14.576 kHz, a significant resonance noise between the stator and rotor was generated, and tiny rotating motion occurred on the rotor. We adjusted the amplitude and frequency, noticing the rotor started to rotate clockwise constantly at 1.5 $V_{p-p}$ and 14.435 kHz. Fig. 4.5 shows the motion captured from the video by each frame. The rotation started and

continued for around 5 seconds, and then stopped.

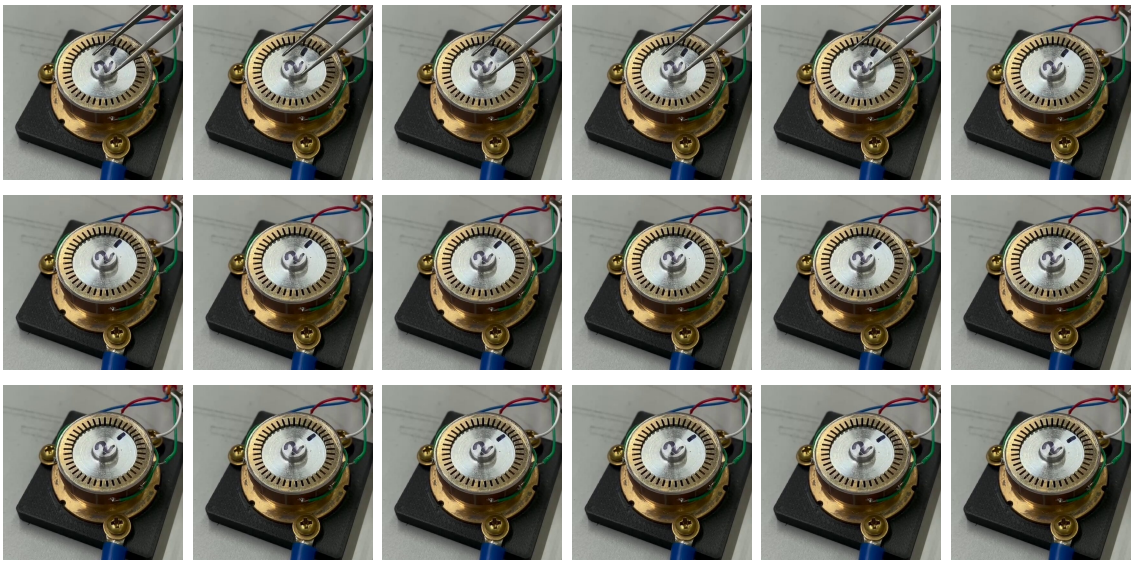

Figure 4.5: Rotor #2 Motion Captured Frame by Frame at 14.435 kHz and 1.5 $V_{p-p}$

As we increased the frequency to the fourth mode around 21.505 kHz, the rotor started to rotate again and the speed of rotation was visibly increased comparing to the motion at the third mode. While adjusting the frequency, we noticed at 21.625 kHz and 1.5 $V_{p-p}$, the rotor reached the fastest speed, as shown in Fig. 4.6.

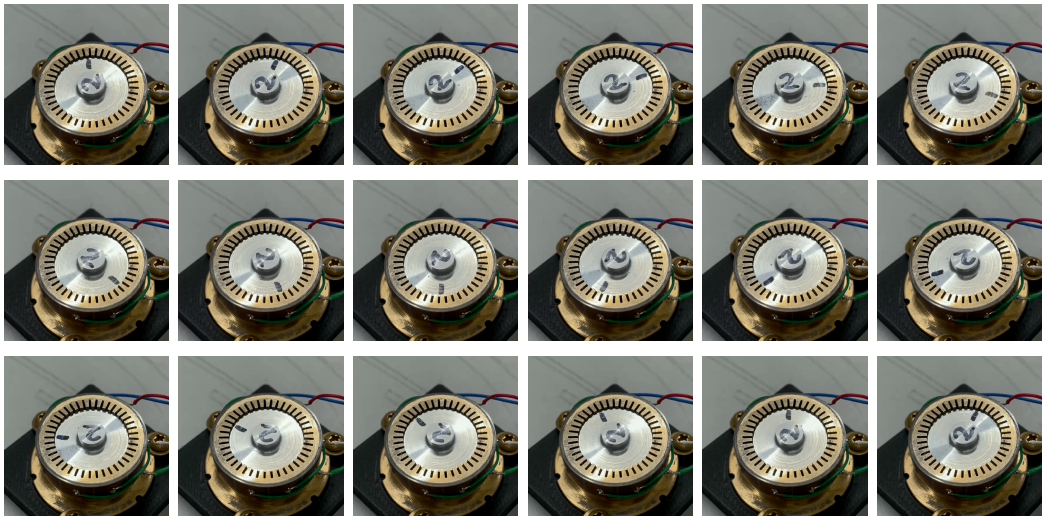

Figure 4.6: Rotor #2 Motion Captured Frame by Frame at 21.625 kHz and 1.5 $V_{p-p}$

The rotor started to rotate at 30.822 kHz. Only 900 $mV_{p-p}$ of amplitude from the waveform generator was provided while the rotor started rotating. The direction of the rotation was counter-clockwise, as shown in Fig 4.7.

Figure 4.7: Rotor #2 Motion Captured Frame by Frame at 30.822 kHz and 900 $mV_{p-p}$

While searching the excitation frequencies around the fifth mode, we noticed the direction of the rotation of the rotor varied at certain frequencies. Table 4.3 shows some of the frequencies that the rotor reached fastest speed before the direction reversed.

| Frequency (kHz) | Rotation Direction |
|---|---|
| 30.925 | Clockwise |
| 31.325 | Counter-Clockwise |
| 31.725 | Clockwise |

Table 4.3: Direction of Rotation at Certain Frequencies

A copper screw, the rotor #1 and #3 and a twenty-gram weight were put on the top of rotor #2 as a weight separately to test the preload impact on the motion of the stator. The total preload was the force generated by the rotor and the weight that applied to the notches, which was perpendicular to the contacting area. Eq. 4.1 shows the calculation formula for preload, and Table 4.4 shows the preload configuration for each setting up.

$$P_L = G \times sin1^\circ \tag{4.1}$$

| Item | Preload $P_L$ ($\times 10^{-4}$N) |
|---|---|
| Rotor #1 | 13.269 |
| Rotor #3 | 8.441 |
| Copper screw | 11.471 |
| Weight | 38.368 |

Table 4.4: Preload Configuration

Fig. 4.8 shows the motion of the rotor while a copper screw was put on as a preload. The frequency and amplitude was set at 21.625 kHz and 1.5 $V_{p-p}$, where the fastest and most constant motion generated within the range of the forth mode from previous experiment.

The speed of rotation increased first, as the change of angle per frame increased, when we put rotor #3. The speed decreased when we removed changed the weight from rotor #3 to copper screw, however, the stability increased. While putting the twenty-gram weight on the rotor, the rotation stopped and could not be actuated. Rotor #3 was slightly oversized by 0.0002" in diameter due to manufacturing tolerance, the contacting area was higher than we expected in Fig. 4.2(c). The frequency

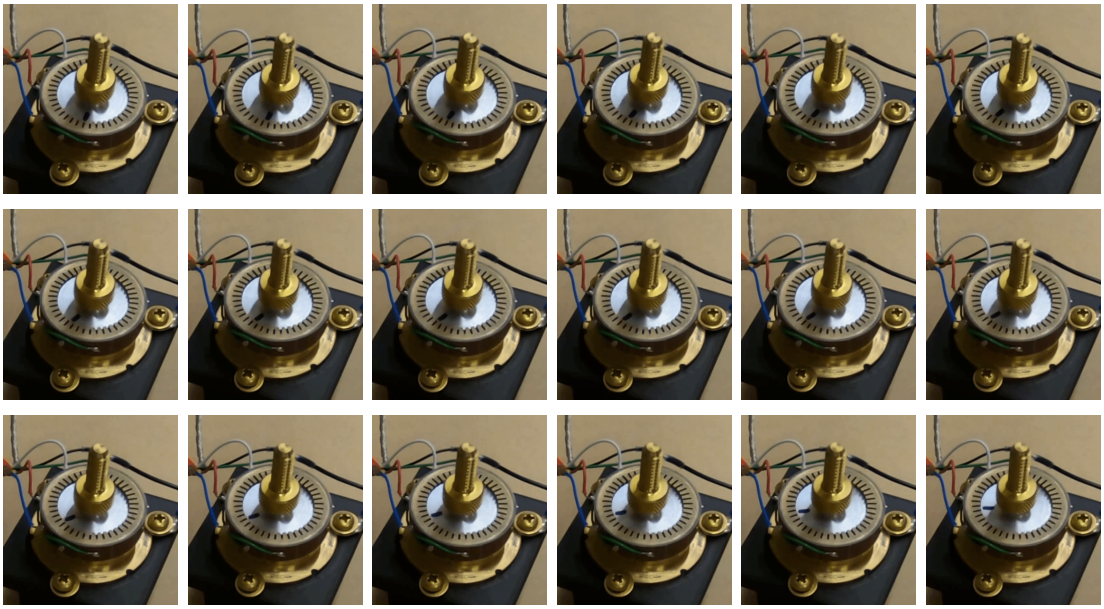

Figure 4.8: Rotor #2 with Preload Captured Frame by Frame at 21.625 kHz and 1.5 $V_{p-p}$

and amplitude was set to 30.822 kHz and 900 mV $_{p-p}$, where was proved as a proper excitation frequency around the fifth drive mode when testing on rotor #2. Fig. 4.9 shows the motion while rotating. The motion was constant and the rotor kept rotating until we cut the power, however, due to the manufacturing tolerance, and lack of constrains like bearings, the motion of rotor #3 was not stable.

Due to manufacturing error, stator #2 was unable to excite any of the rotors. Two of the notches was taller than the others, which stopped the rotor forming up a steady line contact with the stator. The black markers on the stator were the faulted notches that caused the problem, as shown in Fig. 4.10. While putting any of the rotor on, those two spots would contact to the rotor and prevent the other area to form a desired contact model.

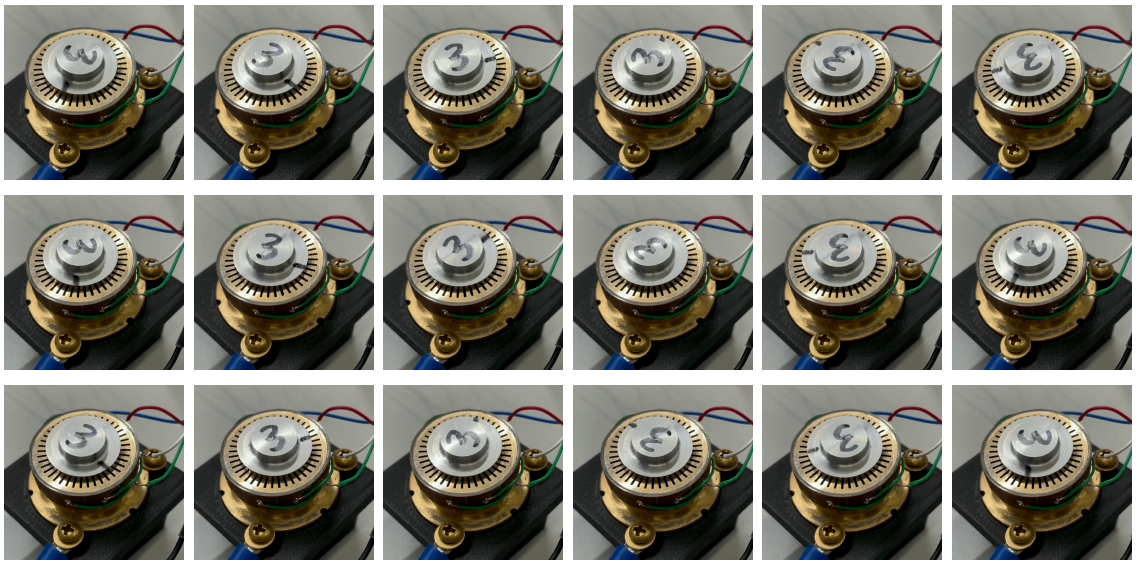

Figure 4.9: Rotor #3 Motion Captured Frame by Frame at 30.822 kHz and 900 $\mathrm{mV}_{p-p}$

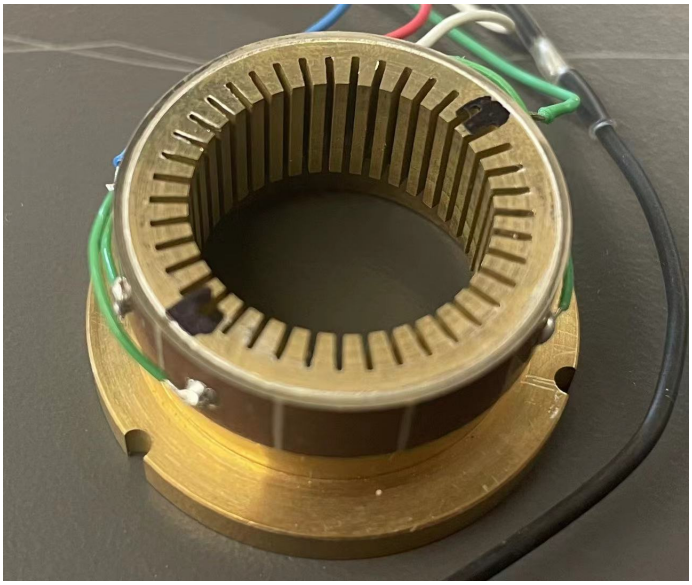

Figure 4.10: Manufacturing Error on Stator #2

## 4.4 Comparison

The study of the impact on different contact model was failed due to the manufacturing tolerance on the stator and rotor #1. Two line contact rotors were rotating constantly at certain excitation frequencies.

While increasing the frequency of the input signal, which means moving from a lower resonance mode to a higher one, the speed of the rotation increased and became more stable.

The gain of the motor is controlled by the voltage of the input power source. As increasing the voltage, the gain increased at the same time. The proposed voltage during simulation was set as 60 $V_{p-p}$, whereas it was for the resonance study of stator assembly so preload was not take into consideration. The experiment on influence of preload indicated that at a certain range of preload force, the increase of preload will increase the speed and stability of the motion, because the rotor design was based on friction coupling method. However, when the preload exceeded the maximum limit, it prevented the rotor from spinning continuously.

Comparing the location of contacting area, rotor #3 which contacting the upper section of the notches was rotating faster than rotor #2, which contacting the bottom section of the area covered by the piezoelectric tube.

# Chapter 5

# DISCUSSION

Fig. 5.1 shows the approximate excitation frequencies comparing to the results from simulation. The maximum of error was only ±2.6%, which indicates the practical experiments on the stator assemblies matched the results from our simulations. Experiments on locating accurate excitation frequencies will be the first step for the future of this research.

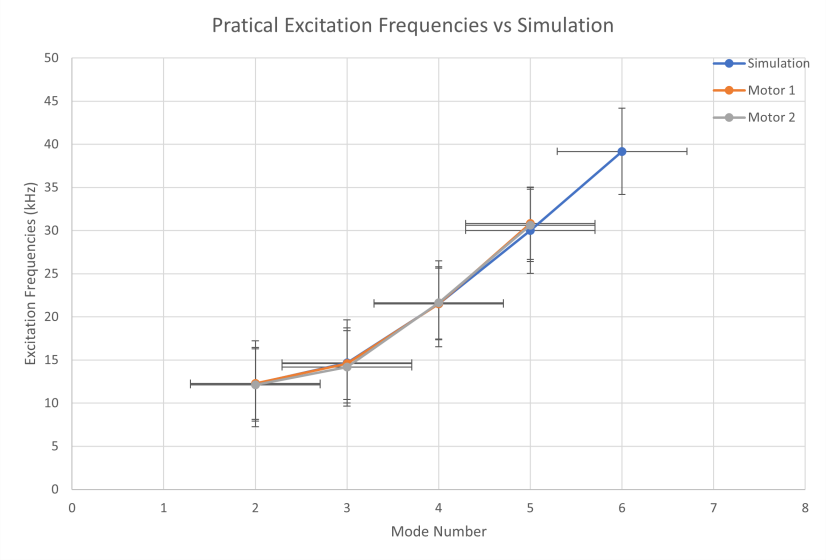


Figure 5.1: Comparison between Practical Result and Simulation

The rotor started to rotate on the third mode at around 14.435 kHz matched our assumption about the motor can be actuated at low frequency. However, the second resonance mode was detected, the gain was too small to actuate the motion.

Comparing to the other semi-customized planar rotary piezoelectric motor, the hollow cylindrical design was able to provide a constant rotation at a lower frequency, and could be self-concentric during rotation.

The stator we presented in this thesis was based on reverse engineering from USR-30 (Shinsei Corporation, Japan). However, there might be some modification to Shinsei's design theory by changing the thickness of the stator wall, the dimension of the notches, the electrode pattern, and so on to optimize the performance of our hollow cylindrical piezoelectric motor. For example, reducing the thickness of the stator wall will increase the flexibility of the stator wall which will also increase the displacement at the top of the notches. Greater displacement at the top of the notches will lead to higher transmission coefficiency between the piezoelectric material and the rotor.

The piezoelectric tube that we originally ordered was 1/2" height, and was cut into 1/4" to match the model that we used in this thesis. However, the cutting process also caused other potential issues. The most important issue was the lost of material, which made the height of our validation model smaller than the simulation motor to around 0.01". The cutting process also made the surface finish of the cutting-plane uncontrollable, which may cause a shorted circuit between the copper layers on the inner and outer surface of the piezoelectric tube. Thus, a surface irregularity might also cause a tip discharge. One of the piezoelectric tubes was destroyed during the first cutting.

In this thesis, most of the part was hand made by ourselves. The manufacturing tolerance was so big that some of the desired mating features were unavailable.

For example, the manufacturing tolerance of the stator has made one of the stators nonfunctional, and the manufacturing tolerance of the tapered rotor also made the experiment on contacting method unsuccessful. The manufacturing method for some of the parts including the stator and rotor could be developed to make it more cost-effective. Current stator manufacturing method contains a great number of manufacturing process on different machinery equipment which increased the tolerance.

As for the contacting method validation, rotor#1 which has the largest contacting surface area, was expected to have the most constant and stable motion among all three rotors. During the experiment on rotor #1, we were able to notice the noise that generated by resonance, however, the rotor could not be actuated at all. We assumed that the vibration of the stator generated by the deformation of piezoelectric tube was absorbed by the TPFE tape.

During the practical experiment, we noticed that the motion of the rotor varied at the same configuration on the waveform generator. With the time increased, the speed and stability of the motion of the rotor was visibly decreased. Then we need to increase the frequency on waveform generator to maintain the same performance. We assumed that was caused by the heat built up within the assembly.

During the adjustment of the frequency, while within the range of a driving mode, the direction that the rotor will be reversed every 400 Hz, which matched the experiment presented in [45]. This circumstance proves that we can change the direction of rotation by changing the frequency while in a certain range within a single resonance mode.

# Chapter 6

# CONCLUSION and Future Work

### 6.0.1 Conclusion

In this thesis, we designed and fabricated a customized stator for a piezoelectric actuator that has a hollow cylindrical shape, and validated it with simulation and practical experiments. A FEM simulation was first used to find the excitation frequencies of the piezoelectric element (PZT-5H) and the displacement of multiple points on the surface of stator assembly where coupling with rotor that we designed. Then, two real stator assemblies with multiple stator prototypes were manufactured to validate the motor performance compared to the simulation. The performance of the real stator assembly matched the simulation results. As raising up the frequency of the stator, the rotating speed and stability of the rotor also increased which matched the simulation results and previous research on plastic customized piezoelectric motor presented in [33]. The spinning speed of the upper section contacting also matched with our simulation results. The stator model that we proposed was proved to be validated.

Chapter 1 introduced some background on MR imaging technique, MRI compatible surgical robotics system, MRI-compatible actuation techniques, commercially avail-

able piezoelectric motors and their operating principles, and piezoelectric traveling wave ultrasonic motor. Also, several hollow cylindrical piezoelectric motors that use different driving means of our design were discussed. A relevant commercial product that has similar design purpose of our hollow cylindrical piezoelectric motor.

Chapter 2 presents the methodologies for modeling the stator assembly. Two prototypes of the stator design were clarified and compared at first. With the design model settled, a material selection process for each part based on the material properties and characteristics was provided. Then, the manufacturing process for the parts was also presented, following the design and dimensions from the model.

Chapter 3 introduces the workspace and model configuration for FEM simulation. The model was imported from SolidWorks to COMSOL and configured according our simulation setup. A cylindrical coordinate system was declared with the respect to the default coordinate system configuration. Three boundary probes were applied to the model to observe the displacement while applying the input signals on the piezoelectric tube. An eigen frequency study and a time domain study were added to the model to find out the resonance modes, corresponding frequencies, and estimated performance of the stator. Then three setups were configured to find the impact on the motor performance when changes were made to our proposed stator design.

Chapter 4 demonstrates the physical test of the stator. A validation of the existence of each resonance mode and its corresponding frequency was performed based on the results we received from simulation. Two stator assemblies were fabricated for comparison. A motor performance validation is presented with a rotor installed on the stator. An experiment on the impact of different contacting method was performed. A preload impact experiment is also presented. The issues in this validation process are discussed and possible explanation is declared.

Chapter 5 provides a discussion on the results and issues we gathered during the whole research process. The results from validation are compared to the simulation, the difference is discussed and possible explanation is proposed.

### 6.0.2 Future Work

The future work on this research should be focus on some of the existing issues and future optimization of the actuator as well. The first step would be building up a cover and add preload as a certain protocol to control the motion of the rotor. Testing with dynamic torque sensor and encoder will provide us the detailed characteristics of the motor. Manufacturing quality including surface roughness and tolerance will also be an important protocol to determine the effect on the performance of the motor.

More studies on changing the pattern of electrodes and notch properties will be performed since all these parameters were reverse engineered from Shinsei's USR30 ultrasonic motor that has a planar rotary shape. Different fabrication methods including the conductive adhesive and electrode connection method will also take place for optimizing the motor.

After solving the existing problems, a more efficient and precise manufacturing method should be discovered for the stator and rotor. And with continues research, scaling up the size of the motor should be also considered to provide more compatibility for other surgical devices.

# Appendix A

# Material Properties

## A.1 PZT-5H

Lead Zirconium Titanate (PZT-5H) Material Properties

| | | | | | | |
|---|---|---|---|---|---|---|
| Elasticity Matrix ($10^{10}Pa$) | 12.721 | 8.021 | 8.467 | 0 | 0 | 0 |
| | 8.021 | 12.721 | 8.467 | 0 | 0 | 0 |
| | 8.467 | 8.467 | 11.744 | 0 | 0 | 0 |
| | 0 | 0 | 0 | 2.299 | 0 | 0 |
| | 0 | 0 | 0 | 0 | 2.299 | 0 |
| | 0 | 0 | 0 | 0 | 0 | 2.347 |
| Coupling Matrix ($C/m^2$) | 0 | 0 | 0 | 0 | 17.035 | 0 |
| | 0 | 0 | 0 | 17.035 | 0 | 0 |
| | -6.623 | -6.623 | 23.240 | 0 | 0 | 0 |
| Relative Permittivity | 1704.4 | | | | | |
| | 1704.4 | | | | | |
| | 1433.6 | | | | | |
| Density ($kg/m^3$) | 7500 | | | | | |

Table A.1: PZT-5H Properties

## A.2 Epoxy

Epoxy Material Properties

| | |
|---|---|
| Young's Modulus | $0.7 * 10^9 Pa$ |
| Poisson Ratio | 0.33 |
| Density | 3500 $kg/m^3$ |

Table A.2: Epoxy Properties

## A.3 Brass C360

Brass C360 Material Properties

| | |
|---|---|
| Young's Modulus | $9.722 * 10^{10} Pa$ |
| Poisson Ratio | 0.311 |
| Density | $8.5 kg/m^3$ |

Table A.3: Brass C360 Properties

## A.4 Aluminum 6061

Aluminum 6061 Material Properties [46]

| | |
|---|---|
| Young's Modulus | $7 * 10^{10} Pa$ |
| Poisson Ratio | 0.33 |
| Density | $2.7 kg/m^3$ |

Table A.4: Aluminum 6061 Properties

# Appendix B

# USR-60RN Properties

Shinsei Corporation USR-60RN Series Hollow Cylindrical Piezoelectric Motor Properties [36]

■Specification

| Model Name | USR60-RN |
|---|---|
| Drive Frequency | 40[KHz]~45[KHz] |
| Drive Voltage | 130[Vrms] |
| Rated Output | 5.0[W] |
| Maximum Output | 10.0[W](by Maximum Load) |
| Rated Speed | 100[rpm] |
| Maximum Speed | 150[rpm] |
| Rated Torque | 0.5[N·m](5.0[Kg·cm]) |
| Maximum Torque | 1.0[N·m](10.0[Kg·cm]) |
| Holding Torque | 1.0[N·m](10.0[Kg·cm]) |
| Response | Less than 1 [ms] ( No-load ) |
| Direction of Rotation | CW, CCW |
| Temperature Range | -10~+55[℃] |
| Temperature Limit | Surface of Stator 70 [℃] |
| Humidity Range | 0~+45[%]( without condensation) |
| Endurance Time | 1,500[Hours] |
| Size | 65×75×30[mm] |
| Weight | 200[g] |
| Remarks | Hole Φ32[mm] |

Figure B.1: USR-60RN Specification

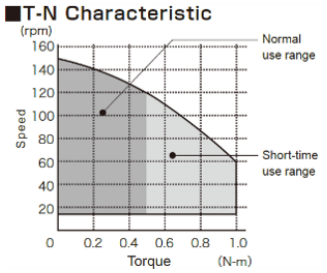


Figure B.2: USR-60RN T-N Characteristic

# Appendix C

# Etching Process

In order to isolate the segments on the piezoelectric tube, an etching process was applied to the outer surface of the tube. An etch process is normally using acid or laser beam to remove the top surface of a hard material. It is a common method when printing PCB circuit boards. Ferric chloride solution from MG Chemicals was used for this process.

According to the pattern on piezoelectric tube we mentioned in Section 3.2, the outer surface of the tube was divided into eleven insulated segments. In order to isolate the segments, narrow gaps between each segment should be built, which means the layer of copper on each gap needs to be removed. A layer of mask was applied to both side of the tube, avoiding unexpected etching on the areas which were used as ground and electrical potentials. An oil based permanent black marker was used to make up as the mask, as shown in Fig. C.1. The gap between each segment were set as 0.02".

With the mask on, the piezoelectric tube was hanged by a piece of iron wire and

Figure C.1: Piezoelectric Tube with Mask on

soaked into the ferric chloride solution for around 45 seconds, as shown in Fig. C.2.

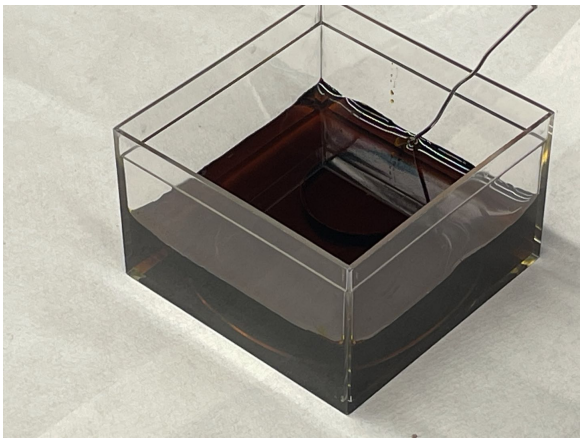

Figure C.2: Soak the Piezoelectric Tube into Ferric Chloride Solution

After soaking in the ferric chloride solution, the tube was put into DI water to clean the residue left on the surface, as shown in Fig. C.3(a). With a dust-free tissue to dry out the surface, acetone was used to clean up the mask, as shown in Fig. C.3(b).

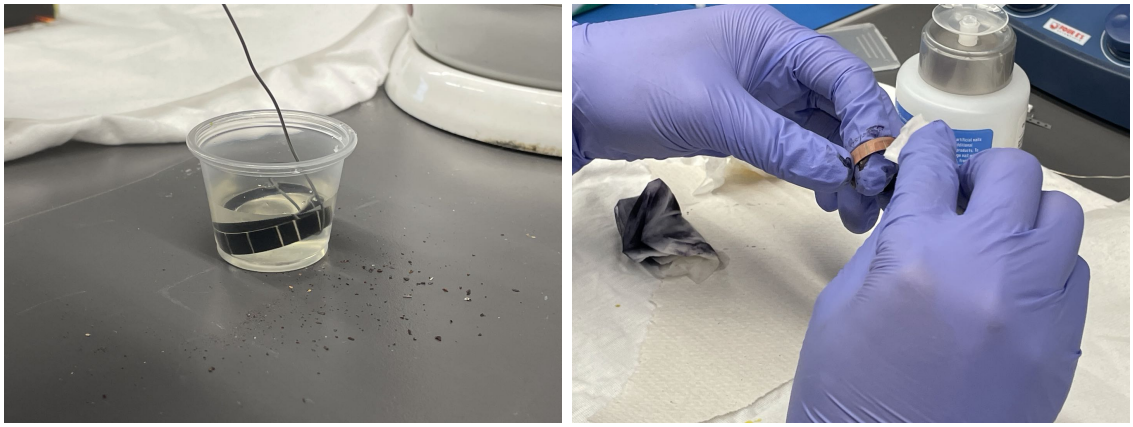

(a) Wash the Tube in DI water (b) Remove the Mask

Figure C.3: Clean the Tube after Etching

After cleaning up the electrodes, an insulation resistance tester from UNI-T (UT501A) was used to check the potential existence of shortage. A voltage at 100V was first applied to check the insulation between each segment on the outer surface, as shown in Fig. C.4(a). A tip discharge would occur if the etch depth was not as expected. Voltage was also applied across the tube wall to check potential shortage caused by the cutting process, as shown in Fig. C.4(b). The whole checking process was repeated with changing the voltage to 500V to observe the reliability as well.

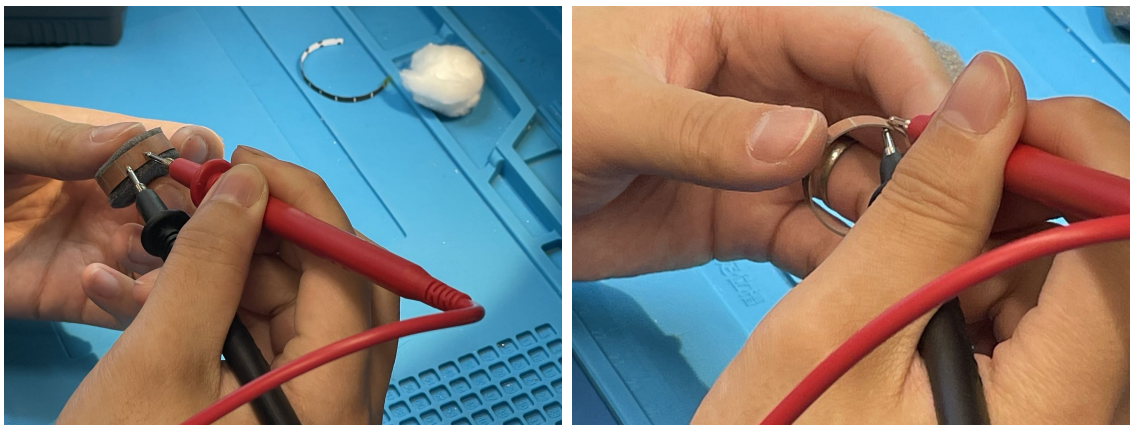

(a) Outer Surface (b) Inner and Outer

Figure C.4: Shortage Check

# Bibliography


[1] B. S. Peters, P. R. Armijo, C. Krause, S. A. Choudhury, and D. Oleynikov, "Review of emerging surgical robotic technology," *Surgical Endoscopy*, 2018.

[2] A. J. Sayari, C. Pardo, B. A. Basques, and M. W. Colman, "Review of robotic-assisted surgery: what the future looks like through a spine oncology lens," *Annals of Translational Medicine*, May 2019.

[3] Y. Chen, S. Zhang, Z. Wu, B. Yang, Q. Luo, and K. Xu *Frontiers of Medicine*, 2020.

[4] R. D. Howe and Y. Matsuoka, "Robotics for surgery," *Annual Review of Biomedical Engineering*, vol. 1, no. 1, pp. 211–240, 1999.

[5] TheEuropeanSpaceAgency, "Mri brain scan."

[6] P. A. Rinck, ed., *Facts and Figures*, ch. 21. 2018-2019.

[7] Statista, "Number of magnetic resonance imaging (mri) units in selected countries as of 2019(per million population)."

[8] Wikipedia, "Electric motor."

[9] A. Fischer, Gregory S.and Krieger, I. Iordachita, C. Csoma, L. L. Whitcomb, and G. Fichtinger, "Mri compatibility of robot actuation techniques – a comparative study," in *Medical Image Computing and Computer-Assisted Intervention – MICCAI 2008* (D. Metaxas, L. Axel, G. Fichtinger, and G. Székely, eds.), (Berlin, Heidelberg), pp. 509–517, Springer Berlin Heidelberg, 2008.

[10] R. Monfaredi, K. Cleary, and K. Sharma, "Mri robots for needle-based interventions: System and technology," *Annals of Biomedical Engineering*, vol. 46, 10 2018.

[11] H. Elhawary, Z. Tse, A. Hamed, M. Rea, B. Davies, and M. Lampérth, "The case for mri compatible robotics: A review of the state of the art," *The international journal of medical robotics + computer assisted surgery : MRCAS*, vol. 4, pp. 105–13, 06 2008.

[12] M. Hashizume, T. Yasunaga, K. Konishi, K. Tanoue, S. Ieiri, K. Kishi, H.Nakamoto, D. Ikeda, I. Sakuma, M. Fujie, and T. Dohi, "New real-time mr image-guided surgical robotic system for minimally invasive precision surgery," *International Journal of Computer Assisted Radiology and Surgery*, vol. 2, 04 2008.

[13] F. J. Siepel, M. K. Welleweerd, V. Groenhuis, S. Stramigioli, B. Maris, and P. Fiorini, "Needle and biopsy robots: a review," *Current Robotics Reports*, 2021.

[14] N. V. Tsekos, A. Khanicheh, E. Christoforou, and C. Mavroidis, "Magnetic resonance-compatible robotic and mechatronics systems for image-guided interventions and rehabilitation: a review study," *Annual review of biomedical engineering*, no. 35-287, 2007.

[15] K. Masamune, E. Kobayashi, Y. Masutani, M. Suzuki, T. Dohi, H. Iseki, and K. Takakura, "Development of an mri-compatible needle insertion manipulator for stereotactic neurosurgery," *Journal of Image Guided Surgery*, vol. 4, 1995.

[16] G. R. Sutherland, I. Latour, and A. D. Greer, ""integrating an image-guided robot with intraoperative mri," *Engineering in Medicine and Biology Magazine*, vol. 27, 2008.

[17] D. B. Comber, E. J. Barth, and R. J. Webster, "Design and control of an magnetic resonance compatible precision pneumatic active cannula robot," *Journal of Medical Devices*, vol. 8, 2014.

[18] C. J. Nycz, R. Gondokaryono, P. Carvalho, N. Patel, M. Wartenberg, J. G. Pilitsis, and G. S. Fischer, "Mechanical validation of an mri compatible stereotactic neurosurgery robot in preparation for pre-clinical trials," *2017 IEEE/RSJ International Conference on Intelligent Robots and Systems (IROS)*, pp. 1677–1684, 2017.

[19] Wikipedia, "Pneumatic actuator."

[20] InstTools, "What is a hydraulic actuator?."

[21] Wikipedia, "Piezoelectric actuator."

[22] R. Firoozian, "Actuators based on electro-rheological fluid," *Servo Motors and Industrial Control Theory*, pp. 119–130, 2009.

[23] H. Kim, S. Oh, K. Hwang, H. Choi, J. Jeon, and J. Nam, "Actuator model of electrostrictive polymers (eps) for microactuators," *Smart Structures and Materials 2001: Electroactive Polymer Actuators and Devices*, July 2001.

[24] N. H. Arbab and F. Najafi, "Stability and performance of pneumatic actuators in impedance control," *Proceedings of the Institution of Mechanical Engineers, Part I: Journal of Systems and Control Engineering*, vol. 228, no. 7, pp. 476–485, 2014.

[25] J. Xiao, Q. Liu, G. Wang, and J. Ji, "Theoretical and experimental analysis of the hydraulic actuator used in the active reflector system," *Mathematical Problems in Engineering*, no. 8503628, 2018.

[26] X. Gong, K. Yang, J. Xie, Y. Wang, P. Kulkarni, A. S. Hobbs, and A. D. Mazzeo, "Rotary actuators based on pneumatically driven elastomeric structures," *Advanced Materials*, June 2016.

[27] InstrumentationTools, "What is a pneumatic actuator?."

[28] Wikipedia, "Electrostrictive polymer."

[29] ShinseiCorporation, "Ultrasonic motor catalog."

[30] PiezoMotor, "Piezo leg linear motor."

[31] PiezoMotion, "Dti motor."

[32] P. A. Carvalho, H. Tang, P. Razavi, K. Pooladvand, W. C. Castro, K. Y. Gandomi, Z. Zhao, C. Nycz, C. Furlong, and G. S. Fishcer, "Study of mri compatible piezoelectric motors by finite element modeling and high-speed digital holography," *Advancement of Optical Methods & Digital Image Correlation in Experimental Mechanics*, vol. 3, pp. 105–112, 2020.

[33] Z. Zhao, P. A. Carvalho, H. Tang, K. Pooladvand, K. Y. Gandomi, C. Nycz, C. Furlong, and G. S. Fishcer, "Preliminary characterization of a plastic piezoelectric motor stator using high-speed digital holographic interferometry," *Advancement of Optical Methods & Digital Image Correlation in Experimental Mechanics*, pp. 89–93, 2021.

[34] ShinseiCorporation, "Ultrasonic motor."

[35] X. Tian, Y. Liu, J. Deng, L. Wang, and W. Chen, "A review on piezoelectric ultrasonic motors for the past decade: Classification, operating principle, performance, and future work perspectives," *Sensors and Actuators A: Physical*, vol. 306, p. 111971, 2020.

[36] ShinseiCorporation, "Ultrasonic motor catalog 2017."

[37] EBLProducts, "Piezoelectric tube properties."

[38] ProtoLabs, "Material selection guide."

[39] P. A. Carvalho, K. Y. Gandomi, C. Nycz, , and G. S. Fishcer, "Multiphysics simulation of an ultrasonic piezoelectric motor," *COMSOL Conference*, 2018.

[40] COMSOL, "Radially polarized piezoelectric transducer."

[41] COMSOL, "About probes."

[42] R. Gabai and I. Bucher, "Spatial and Temporal Excitation to Generate Traveling Waves in Structures," *Journal of Applied Mechanics*, vol. 77, 12 2009.

[43] Holocenter, "What is a hologram?."

[44] Wikipedia, "Holography."

[45] N. S. Vatkar and Y. S. Vatkar, "Piezoelectric motors & it's applications," *International Research Journal of Engineering and Technology*, vol. 03, June 2016.

[46] MIT, "Aluminum 6061 properties."